

Variational Integrators and Graph-Based Solvers for Multibody Dynamics in Maximal Coordinates

Jan Brüdigam^{1*}, Stefan Sosnowski¹, Zachary Manchester²
and Sandra Hirche¹

¹School of Computation, Information and Technology, Technical University of Munich, Barer Str. 21, Munich, 80333, Germany.

²The Robotics Institute, Carnegie Mellon University, 5000 Forbes Avenue, Pittsburgh, 15213, PA, USA.

*Corresponding author(s). E-mail(s): jan.bruedigam@tum.de;
Contributing authors: sosnowski@tum.de; zacm@cmu.edu;
hirche@tum.de;

Abstract

Multibody dynamics simulators are an important tool in many fields, including learning and control for robotics. However, many existing dynamics simulators suffer from inaccuracies when dealing with constrained mechanical systems due to unsuitable integrators and dissatisfying constraint handling. Variational integrators are numerical discretization methods that can reduce physical inaccuracies when simulating mechanical systems, and formulating the dynamics in maximal coordinates allows for easy and numerically robust incorporation of constraints such as kinematic loops or contacts. Therefore, this article derives a variational integrator for mechanical systems with equality and inequality constraints in maximal coordinates. Additionally, efficient graph-based sparsity-exploiting algorithms for solving the integrator are provided and implemented as an open-source simulator. The evaluation of the simulator shows the improved physical accuracy due to the variational integrator and the advantages of the sparse solvers, while application examples of a walking robot and an exoskeleton with explicit constraints demonstrate the necessity and capabilities of maximal coordinates.

Keywords: Maximal Coordinates, Multibody Dynamics, Variational Integrators, Simulation

1 Introduction

Simulators for mechanical systems are widely used, for example in testing and verification [1, 2], model-based control strategies [3, 4], or learning-based methods [5, 6]. However, many common simulators have numerical difficulties with more complex mechanical systems involving constraints. Such constraints can describe kinematic loops, for example in exoskeletons, or they can represent rigid contacts when walking on terrain or grasping objects. To alleviate these numerical issues, simulators often allow small constraint violations, for example by representing all constraints as spring-damper elements as in MuJoCo [7] or Brax [8], or by accepting interpenetration of bodies as in Drake [9] and Bullet [10]. While certain approximations of a real physical system are sometimes necessary and even unavoidable, accepting constraint violation for stable simulations contributes to the sim-to-real gap, a major issue in robotics [11].

Most simulators, including the ones listed above except Brax, use minimal (generalized) coordinates as a mechanism’s state representation. The algorithms typically used for these coordinates may cause numerical issues [12, 13], for example due to their recursive nature, although a rigorous study of the numerical effects and stability of minimal-coordinate dynamics algorithms remains to be done. Additionally, all of the simulators above use numerical integrators for the dynamics that are not well suited for constrained mechanical systems, for example due to the unrealistic energy behavior of explicit or implicit Runge-Kutta methods.

Besides minimal coordinates, so-called maximal coordinates can be used for simulation of constrained mechanical systems. Contrary to minimal coordinates, maximal coordinates represent each body in a mechanism with six degrees of freedom and all kinematic relations such as joints or contacts are represented by explicit constraints. Maximal coordinates allow for the use of direct matrix methods, which generally have well-investigated numerical properties [14]. The few existing works on simulation in maximal coordinates have explored algorithms for continuous-time forward dynamics [15], and discrete-time algorithms for mechanisms without kinematic loops or contacts [16]. Besides their application in simulation, maximal coordinates have shown promising results in control applications [17, 18]. The simulator Brax is also based on maximal coordinates, but suffers from the afore mentioned issues of unsuitable integrators and soft constraint handling.

Suitable integrators for mechanical systems are so-called variational integrators. These integrators are a method for discretizing the differential equations describing a mechanical system while maintaining certain properties such as energy and momentum conservation [19]. Compared to classical discretizations such as explicit Runge-Kutta methods, larger time steps can be taken due to the increased physical accuracy, and constraint drift is avoided entirely. Variational integrators have been theoretically investigated in minimal coordinates [20–22], but the implementations are limited to simple mechanical systems with few joint types and no contact interactions, potentially due to numerical difficulties. Variational integrators in maximal coordinates have

been investigated as well [16, 23], but without formal treatment of kinematic loops or contact interactions.

To address these shortcomings, the contribution of this article for maximal-coordinate simulators is as follows. Firstly, we derive a variational integrator in maximal coordinates for physically accurate simulations including rigid, non-drifting constraints. While variational integrators are generally not new, we derive this integrator in unified framework for common dynamics components including rigid bodies, joints, contacts, friction, actuators and external forces, springs, and dampers. Secondly, we provide an efficient graph-based solver algorithm for the system of nonlinear equations that form the integrator. The solver exploits the sparsity in the nonlinear system of equations to account for the increased number of variables in maximal coordinates. It achieves linear complexity in the number of links and joints for mechanisms without kinematic loops and reduces the complexity for mechanisms with kinematic loops. For environment contacts and friction, the solver also achieves linear complexity in the number of links and contact points while reducing the complexity for inter-mechanism contacts. Besides these theoretical contributions for efficient maximal-coordinate simulators based on variational integrators, we also provide an open-source implementation of such a simulator (see Section 5) which achieves competitive timing results compared to the state-of-the art simulator RigidBodyDynamics [24].

This article is structured as follows. In Section 2, the desired simulator components are mathematically formalized. Based on these components, the variational integrator is derived in Section 3, resulting in a system of nonlinear equations. The solver for this system of equations is presented in Section 4. An evaluation of the theoretical properties and application examples are given in Section 5, and conclusions are drawn in Section 6. The appendices provides background information, including our quaternion notation in Appendix A.

2 Dynamics Components

This section formulates the dynamics components for which the variational integrator is derived in Section 3. Unit quaternions are used for rotations and orientations (see Appendix A for our quaternion notation), but other representations such as rotation matrices could be used as well. Figure 1 shows a mechanism with the treated components.

Rigid Body

In maximal coordinates, each of the n_b rigid bodies in a mechanism has a position $\mathbf{x} \in \mathbb{R}^3$ and orientation $\mathbf{q} \in \mathbb{R}^4$ ($\mathbf{q}^\top \mathbf{q} = 1$), as well as a translational velocity $\mathbf{v} \in \mathbb{R}^3$ and angular velocity $\boldsymbol{\omega} \in \mathbb{R}^3$. The configuration of a body is denoted as $\mathbf{z} = [\mathbf{x}^\top \mathbf{q}^\top]^\top$, and the velocity is denoted as $\dot{\mathbf{z}} = [\mathbf{v}^\top \boldsymbol{\omega}^\top]^\top$. Each body has a mass $m \in \mathbb{R}$ and a symmetric moment of inertia matrix $\mathbf{J} \in \mathbb{R}^{3 \times 3}$. All quantities refer to the center of mass of a body. Given $\mathbf{M} = m\mathbf{I}_{3 \times 3}$, the kinetic energy of each body is $\mathcal{T}(\dot{\mathbf{z}}) = \frac{1}{2}\mathbf{v}^\top \mathbf{M} \mathbf{v} + \frac{1}{2}\boldsymbol{\omega}^\top \mathbf{J} \boldsymbol{\omega}$.

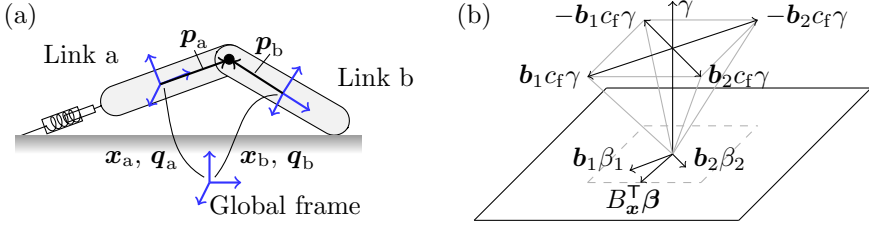


Fig. 1: Exemplary depiction of the simulator components. (a) A two-link mechanism with joints, a spring-damper, and contact subject to friction. (b) A four-sided linearized friction cone.

Conservative Forces, Potentials, and Springs

Conservative forces in the dynamics are derived from potential functions $\mathcal{V}(z_a, z_b, z_c, \dots) \in \mathbb{R}$ involving one or multiple bodies. Such potentials can represent, for example, gravity or springs.

Non-conservative Forces, Actuators, and Dampers

Non-conservative forces including actuators and dampers are directly added to the dynamics as external forces $\mathbf{f} \in \mathbb{R}^3$ or torques $\boldsymbol{\tau} \in \mathbb{R}^3$. Forces are described in the global frame, torques in the body frame. The wrench on a body is denoted as $\mathbf{w} = [\mathbf{f}^T \boldsymbol{\tau}^T]^T$. These wrenches are added for each body individually. Actuators fixed at joints are formulated by expressing their wrench in the frames of the connected bodies. As an example, for an actuator with wrench $\mathbf{w}_{\text{act}} = [\mathbf{f}_{\text{act}}^T \boldsymbol{\tau}_{\text{act}}^T]^T$ at a joint between bodies a (parent) and b (child), the resulting wrenches for the bodies are

$$\mathbf{w}_a = \begin{bmatrix} {}^N\mathbf{f}_a \\ {}^A\boldsymbol{\tau}_a \end{bmatrix} = - \begin{bmatrix} {}^N\mathbf{f}_{\text{act}} \\ {}^A\boldsymbol{\tau}_{\text{act}} + {}^A\mathbf{p}_a \times {}^A\mathbf{f}_{\text{act}} \end{bmatrix}, \quad (1a)$$

$$\mathbf{w}_b = \begin{bmatrix} {}^N\mathbf{f}_b \\ {}^B\boldsymbol{\tau}_b \end{bmatrix} = \begin{bmatrix} {}^N\mathbf{f}_{\text{act}} \\ {}^B\boldsymbol{\tau}_{\text{act}} + {}^B\mathbf{p}_b \times {}^B\mathbf{f}_{\text{act}} \end{bmatrix}, \quad (1b)$$

where N is the global frame, A and B are reference frames of bodies a and b, respectively, and \mathbf{p} is a vector from center of mass to actuator.

Joints and Equality Constraints

The joints of a mechanism consisting of one or multiple rigid bodies are represented by differentiable equality constraints $\mathbf{g}(z_a, z_b, z_c, \dots) = \mathbf{0} \in \mathbb{R}^{n_e}$, where n_e is the number of equality constraints on the mechanism. Typically, equality constraints are formulated for all i kinematically connected pairs of rigid bodies independently and subsequently stacked into one constraint function $\mathbf{g} = [\mathbf{g}_1^T \dots \mathbf{g}_i^T]^T$. In maximal coordinates, two generic equality constraint functions, one for the translational and one for the rotational movement of the two connected bodies, can be combined to create most of the common joints

encountered in mechanisms (see Appendix B for a list of these joints). This insight greatly simplifies analytic gradient calculations for fast computations and gives direct access to minimal coordinates as well.

Contacts and Inequality Constraints

Rigid contacts between multiple bodies and with the environment are represented by differentiable inequality constraints $\phi(\mathbf{z}_a, \mathbf{z}_b, \mathbf{z}_c, \dots) \geq \mathbf{0} \in \mathbb{R}^{n_i}$, where n_i is the number of inequality constraints on the mechanism. As for joints, inequality constraints are typically formulated independently for all j pairs of rigid bodies from their signed distance function and subsequently stacked into one constraint function $\phi = [\phi_1^\top \dots \phi_j^\top]^\top$. Ground contact of a single point contact on a body in maximal coordinates always has the form $\phi(\mathbf{z}) = \mathbf{e}_z^\top(\mathbf{x} + \mathbf{q} \cdot \mathbf{p} \cdot \mathbf{q}^{-1}) \geq 0$, where \mathbf{e}_z is the z-axis unit vector in the global frame and $\mathbf{p} \in \mathbb{R}^3$ points from center of mass to contact point in the body's frame. As before, this consistent structure allows for the calculation of analytic gradients to improve computation time.

Static and Sliding Friction

In the dynamics, static and sliding friction are derived from the maximum dissipation principle [25] with a linearized friction cone [26]. A nonlinear friction cone could be used as well. In our formulation, each contact point involves at most two bodies. An individual optimization problem is formulated for each contact point. The maximum dissipation principle states that the friction force $\beta \in \mathbb{R}^{2n_f}$ maximizes the kinetic energy dissipation rate of the bodies in contact. This principle yields an optimization problem for two bodies a and b:

$$\min_{\beta} \frac{d}{dt} (\mathcal{T}(\dot{\mathbf{z}}_a) + \mathcal{T}(\dot{\mathbf{z}}_b)) = \min_{\beta} \dot{\mathbf{z}}_a^\top \mathbf{B}(\mathbf{z}_a)^\top \beta - \dot{\mathbf{z}}_b^\top \mathbf{B}(\mathbf{z}_b)^\top \beta, \quad (2a)$$

$$\text{s.t. } \mathbf{1}^\top \beta \leq \gamma c_f, \quad (2b)$$

$$\beta \geq \mathbf{0}, \quad (2c)$$

where $\mathbf{1}^\top \beta \leq \gamma c_f$ with $\mathbf{1} = [1 \dots 1]^\top \in \mathbb{R}^{2n_f}$, normal force $\gamma \in \mathbb{R}$, and friction coefficient $c_f \in \mathbb{R}$ describes the limit on the friction force. The matrix $\mathbf{B}(\mathbf{z})^\top = [\mathbf{B}_x \ \mathbf{B}_q]^\top$ consisting of

$$\mathbf{B}_x^\top = [\mathbf{b}_1 \ -\mathbf{b}_1 \ \dots \ \mathbf{b}_{n_f} \ -\mathbf{b}_{n_f}] \in \mathbb{R}^{3 \times 2n_f}, \quad (3a)$$

$$\mathbf{B}_q(\mathbf{q})^\top = \mathbf{p}^\times \mathbf{V} \mathbf{L}(\mathbf{q}) \mathbf{R}(\mathbf{q})^\top \mathbf{V}^\top \mathbf{B}_x^\top \in \mathbb{R}^{3 \times 2n_f}, \quad (3b)$$

maps the friction force β to a six-dimensional wrench on the respective body. The force of this wrench is obtain from mapping with \mathbf{B}_x , and the torque from mapping with \mathbf{B}_q . The vector from center of mass to contact point is denoted \mathbf{p} and the \times operator creates the skew-symmetric matrix this vector. The basis vectors \mathbf{b}_i of the linearized friction cone are depicted in Fig. 1. Note

that the minus sign appears in the cost function because the same friction force β acts in opposite directions on both bodies. For a single body in contact with the environment, only the dissipation rate of this single body needs to be considered in the optimization problem.

3 Mathematical Integrator

A first-order variational (symplectic) integrator [19] is derived for the simulator components described in the previous section. This integrator discretizes the rigid-body dynamics while maintaining energy and momentum conservation properties as well as constraint satisfaction. Higher-order variational integrators are possible [27, 28] and we restrict the derivation to first order for clarity. First, the derivation for unconstrained dynamics is provided. Afterwards, equality and inequality constraints are added to the integrator, and finally friction dynamics are incorporated.

3.1 Unconstrained Dynamics

The derivation of the integrator for unconstrained dynamics is split into translational and rotational components for clarity. Note that the derivation also holds for coupled translational and rotational dynamics. Variational integrators are based on the principle of least action which states that a mechanical system takes the path of least action when going from a fixed start point to a fixed end point. Action has the dimensions [Energy] \times [Time] and the unconstrained action integral S_0 is defined as

$$S_0(\mathbf{z}, \dot{\mathbf{z}}) = \int_{t_0}^{t_N} \mathcal{L}(\mathbf{z}, \dot{\mathbf{z}}) dt + \int_{t_0}^{t_N} [\mathbf{f}^\top \mathbf{2L}(\mathbf{q}) \mathbf{V}^\top \boldsymbol{\tau}]^\top \mathbf{z} dt, \quad (4)$$

where $\mathcal{L} = \mathcal{T} - \mathcal{V}$ is the Lagrangian with kinetic energy \mathcal{T} and potential energy \mathcal{V} . A brief explanation of the torque component in (4) as well as our quaternion notation are given in Appendix A. Further details on virtual work for quaternions can be found in [29, 30].

Translational Component

The translational component of the action integral (4) is

$$S_{0,T}(\mathbf{x}, \mathbf{v}) = \int_{t_0}^{t_N} \mathcal{L}_T(\mathbf{x}, \mathbf{v}) dt + \int_{t_0}^{t_N} \mathbf{f}^\top \mathbf{x} dt. \quad (5)$$

For numerical integration, (5) is discretized. A first-order discretization of the integral and a first-order approximation of the velocity,

$$\mathbf{v}_k = \frac{\mathbf{x}_{k+1} - \mathbf{x}_k}{\Delta t}, \quad (6)$$

with time step Δt is used to obtain the discrete action sum

$$S_{d,0,T}(\mathbf{x}_k, \mathbf{v}_k) = \sum_{k=0}^{N-1} \left(\mathcal{L}_T(\mathbf{x}_k, \mathbf{v}_k) + \mathbf{f}_k^\top \mathbf{x}_k \right) \Delta t. \quad (7)$$

For a first-order integrator, the principle of least action must be fulfilled for trajectories consisting of three knot points, i.e., from 0 to $N = 2$. Since \mathbf{x}_0 and \mathbf{x}_2 are fixed start and end points of the trajectory, only \mathbf{x}_1 can vary. Therefore, the action sum is minimized with respect to the position \mathbf{x}_1 :

$$\nabla_{\mathbf{x}_1} S_{d,0,T} = -\mathbf{d}_{0,T} \Delta t = \mathbf{0}, \quad (8)$$

where $\mathbf{d}_{0,T}$ are the resulting implicit discretized translational dynamics. In words, if equation (8) is fulfilled, we have found the discrete approximation of the physically correct trajectory consisting of the knot points \mathbf{x}_0 , \mathbf{x}_1 , and \mathbf{x}_2 . Note that the derivative with respect to \mathbf{x}_1 is taken for each body in a mechanism.

An example for a single body with potential function $\mathcal{V}(\mathbf{x})$ yields

$$\begin{aligned} \mathbf{d}_{0,T}(\mathbf{v}_1) &= -\nabla_{\mathbf{x}_1} \left(\mathcal{L}_T(\mathbf{x}_0, \mathbf{v}_0) + \mathbf{f}_0^\top \mathbf{x}_0 + \mathcal{L}_T(\mathbf{x}_1, \mathbf{v}_1) + \mathbf{f}_1^\top \mathbf{x}_1 \right) \\ &= - \left(M \frac{\mathbf{x}_1 - \mathbf{x}_0}{\Delta t} - M \frac{\mathbf{x}_2 - \mathbf{x}_1}{\Delta t} - \nabla_{\mathbf{x}_1} \mathcal{V}(\mathbf{x}_1) + \mathbf{f}_1 \right) \\ &= M \frac{\mathbf{v}_1 - \mathbf{v}_0}{\Delta t} + \nabla_{\mathbf{x}_1} \mathcal{V}(\mathbf{x}_1) - \mathbf{f}_1 = \mathbf{0}, \end{aligned} \quad (9)$$

which resembles the discretized version of Newton's second law, $M\dot{\mathbf{v}} - \mathbf{f} = \mathbf{0}$.

The physically accurate dynamics are obtained by varying \mathbf{x}_1 with fixed \mathbf{x}_0 and \mathbf{x}_2 . However, when integrating dynamics forward in time, we start from a known initial state \mathbf{x}_0 and \mathbf{v}_0 . From (6), the position at the next time step, \mathbf{x}_1 , is calculated as

$$\mathbf{x}_1 = \mathbf{x}_0 + \mathbf{v}_0 \Delta t. \quad (10)$$

Then, the implicit dynamics equations (8) are solved to obtain the velocity \mathbf{v}_1 .

Rotational Component

The rotational component of the integrator can be derived similarly to the translation case. A description for an unconstrained floating single rigid body is presented in [23] and we later extend the derivation to constrained multibody systems.

The action integral for the rotational component is

$$S_{0,R}(\mathbf{q}, \boldsymbol{\omega}) = \int_{t_0}^{t_N} \mathcal{L}_R(\mathbf{q}, \boldsymbol{\omega}) dt + \int_{t_0}^{t_N} 2\boldsymbol{\tau}^\top \mathbf{V} \mathbf{L}(\mathbf{q})^\top \mathbf{q} dt. \quad (11)$$

To maintain unit norm in the quaternion update (see Appendix A), the discrete quaternion angular velocity is defined as

$$\bar{\omega}_k = \begin{bmatrix} \sqrt{\left(\frac{2}{\Delta t}\right)^2 - \omega_k^\top \omega_k} \\ \omega_k \end{bmatrix} = 2 \frac{\mathbf{q}_k^{-1} \cdot \mathbf{q}_{k+1}}{\Delta t}. \quad (12)$$

As before, the action integral (11) is discretized to obtain the action sum

$$S_{d,0,R}(\mathbf{q}_k, \omega_k) = \sum_{k=0}^{N-1} (\mathcal{L}_R(\mathbf{q}_k, \omega_k) + 2\tau_k^\top \mathbf{V} \mathbf{L}(\mathbf{q}_k)^\top \mathbf{q}_k) \Delta t. \quad (13)$$

The principle of least action is fulfilled by minimizing the discrete action sum from 0 to $N = 2$ over the orientation \mathbf{q}_1 :

$$\nabla_{\mathbf{q}_1}^\top S_{d,0,R} = -\mathbf{d}_{0,R} \Delta t = \mathbf{0}, \quad (14)$$

where $\mathbf{d}_{0,R}$ are the implicit discretized rotational dynamics. Note that we have used the rotational gradient ∇^\top (see Appendix A), and that the derivative with respect to \mathbf{q}_1 is taken for each body in a mechanism.

An example for a single body with potential function $\mathcal{V}(\mathbf{q})$ yields

$$\begin{aligned} \mathbf{d}_{0,R}(\omega_1) &= \mathbf{J} \omega_1 \sqrt{\frac{4}{\Delta t^2} - \omega_1^\top \omega_1} + \omega_1^\times \mathbf{J} \omega_1 - \\ &\quad \mathbf{J} \omega_0 \sqrt{\frac{4}{\Delta t^2} - \omega_0^\top \omega_0} + \omega_0^\times \mathbf{J} \omega_0 + \nabla_{\mathbf{q}_1}^\top \mathcal{V}(\mathbf{q}_1) - 2\tau_2 = \mathbf{0}, \end{aligned} \quad (15)$$

which—analogueous to the translational case—bears resemblance to Euler's equations for rotations $\mathbf{J} \dot{\omega} + \omega^\times \mathbf{J} \omega - \tau = \mathbf{0}$.

An integration step given \mathbf{q}_0 and ω_0 is performed by first calculating

$$\mathbf{q}_1 = \frac{\Delta t}{2} \mathbf{L}(\mathbf{q}_0) \bar{\omega}_0, \quad (16)$$

and subsequently solving (14) for the angular velocity ω_1 .

3.2 Equality Constrained Dynamics

Equality constraint functions $\mathbf{g}(\mathbf{z})$ with virtual constraint forces $\boldsymbol{\lambda} \in \mathbb{R}^{n_e}$ are added to the integrator by appending them to the action integral:

$$S(\mathbf{z}, \dot{\mathbf{z}}, \boldsymbol{\lambda}) = S_0(\mathbf{z}, \dot{\mathbf{z}}) + \int_{t_0}^{t_N} \boldsymbol{\lambda}^\top \mathbf{g}(\mathbf{z}) \, dt. \quad (17)$$

The virtual constraint forces $\boldsymbol{\lambda}$ act on a rigid body to guarantee satisfaction of constraints $\mathbf{g} = \mathbf{0}$. They are called virtual as they are workless and do not

change the energy of a body. Mathematically, they serve a similar purpose as Lagrange multipliers in constrained optimization.

The discrete action sum changes to

$$S_d(\mathbf{z}_k, \dot{\mathbf{z}}_k, \boldsymbol{\lambda}_k) = S_{d,0}(\mathbf{z}_k, \dot{\mathbf{z}}_k) + \sum_{k=0}^{N-1} \boldsymbol{\lambda}_k^\top \mathbf{g}(\mathbf{z}_k) \Delta t. \quad (18)$$

Taking the gradient of (18) with respect to \mathbf{x}_1 and \mathbf{q}_1 yields the constrained implicit discretized dynamics

$$\mathbf{d}(\dot{\mathbf{z}}_1, \boldsymbol{\lambda}_1) = \mathbf{d}_0(\dot{\mathbf{z}}_1) - \mathbf{G}(\mathbf{z}_1)^\top \boldsymbol{\lambda}_1 = \mathbf{0}, \quad (19a)$$

$$\mathbf{g}(\mathbf{z}_2(\dot{\mathbf{z}}_1)) = \mathbf{0}, \quad (19b)$$

where

$$\mathbf{G}(\mathbf{z}) = \begin{bmatrix} \frac{\partial \mathbf{g}(\mathbf{z})}{\partial \mathbf{x}} & \frac{\partial \mathbf{g}(\mathbf{z})}{\partial^r \mathbf{q}} \end{bmatrix}. \quad (20)$$

The integration step starting from \mathbf{z}_0 and $\dot{\mathbf{z}}_0$ is calculated as follows. First, \mathbf{z}_1 is calculated from the update rules (10) and (16). Then, the nonlinear system of equations (19) is solved for $\dot{\mathbf{z}}_1$ and $\boldsymbol{\lambda}_1$. Note that the constraints are fulfilled for \mathbf{z}_2 which depends on $\dot{\mathbf{z}}_1$ through update rules (10) and (16). Therefore, the resulting velocity $\dot{\mathbf{z}}_1$ always ensures constraint satisfaction for the next position \mathbf{z}_2 .

3.3 Inequality Constrained Dynamics

Inequality constraint functions $\phi(\mathbf{z})$ with constraint forces $\boldsymbol{\gamma} \in \mathbb{R}^{n_i}$ are added to the integrator in a similar fashion. Physically, the constraint forces $\boldsymbol{\gamma}$ are the normal forces at the contacts. To add the constraints to the dynamics, they are discretized and formulated as a nonlinear complementarity problem (NCP)

$$\phi(\mathbf{z}_k) \geq \mathbf{0}, \quad (21a)$$

$$\boldsymbol{\gamma}_k \geq \mathbf{0}, \quad (21b)$$

$$\phi(\mathbf{z}_k)^\top \boldsymbol{\gamma}_k = \mathbf{0}, \quad (21c)$$

with element-wise \geq , for which we use the standard shorthand notation

$$\mathbf{0} \leq \phi(\mathbf{z}_k) \perp \boldsymbol{\gamma}_k \geq \mathbf{0}. \quad (22)$$

The resulting dynamics are

$$\mathbf{d}(\dot{\mathbf{z}}_1, \boldsymbol{\gamma}_1) = \mathbf{d}_0(\dot{\mathbf{z}}_1) - \mathbf{N}(\mathbf{z}_1)^\top \boldsymbol{\gamma}_1 = \mathbf{0}, \quad (23a)$$

$$\mathbf{0} \leq \phi(\mathbf{z}_2(\dot{\mathbf{z}}_1)) \perp \boldsymbol{\gamma}_1 \geq \mathbf{0}, \quad (23b)$$

where

$$\mathbf{N}(\mathbf{z}) = \begin{bmatrix} \frac{\partial \phi(\mathbf{z})}{\partial \mathbf{x}} & \frac{\partial \phi(\mathbf{z})}{\partial^r \mathbf{q}} \end{bmatrix}. \quad (24)$$

The integration step starting from \mathbf{z}_0 and $\dot{\mathbf{z}}_0$ is again performed by first calculating \mathbf{z}_1 from (10) and (16), and then solving (23) for $\dot{\mathbf{z}}_1$ and $\boldsymbol{\gamma}_1$.

3.4 Friction Dynamics

The friction dynamics are included in the variational integrator by discretizing the maximum dissipation principle (2):

$$\min_{\boldsymbol{\beta}} \dot{\mathbf{z}}_{\mathbf{a},k}^\top \mathbf{B}(\mathbf{z}_{\mathbf{a},k})^\top \boldsymbol{\beta}_k - \dot{\mathbf{z}}_{\mathbf{b},k}^\top \mathbf{B}(\mathbf{z}_{\mathbf{b},k})^\top \boldsymbol{\beta}_k, \quad (25a)$$

$$\text{s.t.} \quad \mathbf{1}^\top \boldsymbol{\beta}_k \leq \gamma_k c_f, \quad (25b)$$

$$\boldsymbol{\beta}_k \geq \mathbf{0}. \quad (25c)$$

As with the contact constraint, we formulate (25) as an NCP with Lagrange multipliers ψ_k —the tangential velocity at the contact point—and $\boldsymbol{\eta}_k$:

$$\mathbf{B}(\mathbf{z}_{\mathbf{a},k})\dot{\mathbf{z}}_{\mathbf{a},k} - \mathbf{B}(\mathbf{z}_{\mathbf{b},k})\dot{\mathbf{z}}_{\mathbf{b},k} + \mathbf{1}\psi_k - \boldsymbol{\eta}_k = \mathbf{0}, \quad (26a)$$

$$0 \leq c_f \gamma_k - \mathbf{1}^\top \boldsymbol{\beta}_k \perp \psi_k \geq 0, \quad (26b)$$

$$\mathbf{0} \leq \boldsymbol{\beta}_k \perp \boldsymbol{\eta}_k \geq \mathbf{0}. \quad (26c)$$

The complete integrator including equality constraints, inequality constraints, and friction dynamics is stated in the next subsection.

3.5 Complete Integrator

Putting all components together, the simulation of one time step given \mathbf{z}_0 and $\dot{\mathbf{z}}_0$ is performed by first calculating \mathbf{z}_1 from (10) and (16). Subsequently, the constrained implicit dynamics must be solved:

$$\mathbf{d}(\dot{\mathbf{z}}_1, \boldsymbol{\lambda}_1, \boldsymbol{\gamma}_1, \boldsymbol{\beta}_1) = \mathbf{d}_0(\dot{\mathbf{z}}_1) - \mathbf{G}^\top \boldsymbol{\lambda}_1 - \mathbf{N}^\top \boldsymbol{\gamma}_1 - \mathbf{B}^\top \boldsymbol{\beta}_1 = \mathbf{0}, \quad (27a)$$

$$\mathbf{g}(\mathbf{z}_2(\dot{\mathbf{z}}_1)) = \mathbf{0}, \quad (27b)$$

$$\mathbf{0} \leq \phi(\mathbf{z}_2(\dot{\mathbf{z}}_1)) \perp \boldsymbol{\gamma}_1 \geq \mathbf{0}, \quad (27c)$$

$$\mathbf{B}\dot{\mathbf{z}}_1 + \mathbf{E}\boldsymbol{\psi}_1 - \boldsymbol{\eta}_1 = \mathbf{0}, \quad (27d)$$

$$0 \leq c_f \gamma_1 - \mathbf{E}^\top \boldsymbol{\beta}_1 \perp \boldsymbol{\psi}_1 \geq 0, \quad (27e)$$

$$\mathbf{0} \leq \boldsymbol{\beta}_1 \perp \boldsymbol{\eta}_1 \geq \mathbf{0}, \quad (27f)$$

where $\mathbf{E} = \text{blockdiag}(\mathbf{1}, \dots, \mathbf{1})$. Note that (27) contains the equations and constraints for all bodies of a mechanism and \mathbf{B} consists of the stacked \mathbf{B} matrices of each contact point.

4 Numerical Solver

The variational integrator (27) can be summarized as a system of nonlinear equations with inequality constraints:

$$\mathbf{f}(\mathbf{s}) = \mathbf{0}, \quad (28a)$$

$$\mathbf{h}(\mathbf{s}) \geq \mathbf{0}, \quad (28b)$$

where $\mathbf{s} = [\dot{\mathbf{z}}_1^\top \boldsymbol{\lambda}_1^\top \boldsymbol{\gamma}_1^\top \boldsymbol{\beta}_1^\top \boldsymbol{\psi}_1^\top \boldsymbol{\eta}_1^\top]^\top$. In this section, the algorithms derived for solving the system (28) are applicable for the class of Newton-based root-finding methods. Certain methods of this class, for example interior-point methods [31], introduce slack variables to treat the inequality constraints. In this case, \mathbf{s} would be extended by such slack variables, but the following graph-based argument formulated for the algorithms still holds. Moreover, this graph-based argument is not limited to mechanical systems, but can be implemented for any graph-based system, but we will restrict the discussion to mechanical systems.

At the core, Newton-based methods iteratively produce solution approximations for (28) with the procedure

$$\mathbf{s}^{(i+1)} = \mathbf{s}^{(i)} - \mathbf{F}(\mathbf{s}^{(i)})^{-1} \mathbf{f}(\mathbf{s}^{(i)}), \quad (29)$$

where

$$\mathbf{F}(\mathbf{s}) = \frac{\partial \mathbf{f}(\mathbf{s})}{\partial \mathbf{s}}. \quad (30)$$

Numerically, (29) is formulated as a linear system of equations

$$\mathbf{F}(\mathbf{s}^{(i)}) \Delta \mathbf{s}^{(i)} = -\mathbf{f}(\mathbf{s}^{(i)}), \quad (31)$$

where the result $\Delta \mathbf{s}^{(i)}$ is used to obtain $\mathbf{s}^{(i+1)} = \mathbf{s}^{(i)} + \Delta \mathbf{s}^{(i)}$.

Linear systems of the form (31) are solved with decomposition and back-substitution with overall cubic complexity $\mathcal{O}(n^3)$. For general integrators, including the variational integrator derived in the previous section, (31) is neither symmetric nor block symmetric. Therefore, the LDU decomposition [32] for unsymmetric systems is chosen as the foundation of the algorithms. While (31) is unsymmetric, its sparsity pattern, i.e., the zero and non-zero entries, is block-symmetric, and the following algorithms exploit this sparsity to improve on the complexity.

4.1 Linear-Complexity Algorithm

For mechanisms without kinematic loops the LDU decomposition can be modified to obtain decomposition and backsubstitution with linear complexity $\mathcal{O}(n)$, where n is the number of nodes in the corresponding graph. This modification is achieved by taking into account the graph representing the components of a mechanism and its associated \mathbf{F} matrix. Consider, for example, the mechanism and graph in Fig. 2.

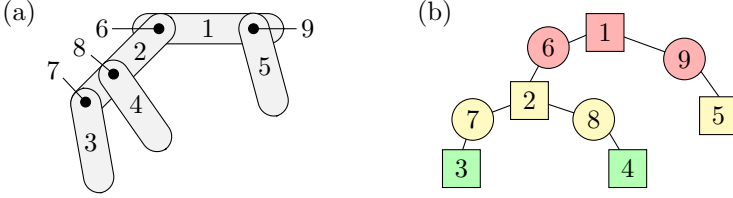


Fig. 2: (a) A mechanism with five links and four joints. (b) A graph representing the mechanism and its matrix. Squares represent links, circles represent joints. Coloring represents different levels of the tree-shaped graph.

According to [33], the \mathbf{F} matrix corresponding to an acyclic graph, i.e., a mechanism without kinematic loops, can be decomposed with linear complexity by traversing the graph from leaves to root.

A depth-first search (DFS) starting from the (arbitrary) root is performed to find the correct processing order. The found nodes are stored in a list with the root as the last element and the last-found node as the first element. This list is then used in the modified LDU decomposition (Algorithm 1) and backsubstitution (Algorithm 2).

Algorithm 1 Sparse In-Place LDU Decomposition, Complexity $\mathcal{O}(n)$

```

1: for  $i \in \text{list}$  do                                      $\triangleright$  list from DFS
2:   for  $c \in \text{children}(i)$  do                              $\triangleright$  children from DFS
3:      $\mathbf{F}_{i,c} \leftarrow \mathbf{F}_{i,c} \mathbf{F}_{c,c}^{-1}$ 
4:      $\mathbf{F}_{c,i} \leftarrow \mathbf{F}_{c,c}^{-1} \mathbf{F}_{c,i}$ 
5:      $\mathbf{F}_{i,i} \leftarrow \mathbf{F}_{i,i} - \mathbf{F}_{i,c} \mathbf{F}_{c,c} \mathbf{F}_{c,i}$ 
6:   end for
7: end for

```

Algorithm 2 Sparse In-Place LDU Backsubstitution, Complexity $\mathcal{O}(n)$

```

1: for  $i \in \text{list}$  do
2:    $\Delta \mathbf{s}_i \leftarrow -\mathbf{f}_i$ 
3:   for  $c \in \text{children}(i)$  do
4:      $\Delta \mathbf{s}_i \leftarrow \Delta \mathbf{s}_i - \mathbf{F}_{i,c} \Delta \mathbf{s}_c$ 
5:   end for
6: end for
7: for  $i \in \text{reverse}(\text{list})$  do
8:    $\Delta \mathbf{s}_i \leftarrow \mathbf{F}_{i,i}^{-1} \Delta \mathbf{s}_i$ 
9:    $\Delta \mathbf{s}_i \leftarrow \Delta \mathbf{s}_i - \mathbf{F}_{c,\text{parent}(i)} \Delta \mathbf{s}_{\text{parent}(i)}$   $\triangleright$  ignore if  $\text{parent}(i) = \emptyset$ 
10: end for

```

The decomposition in Algorithm 1 processes the matrix \mathbf{F} according to the graph structure from leaves to root. Additionally, for each node, computations are only performed for connected components, since computations for unconnected components are zero in the LDU decomposition. The linear complexity is a direct result.

Decomposition Complexity: In an acyclic graph with n nodes, each node has at most one parent, so there are $\mathcal{O}(n)$ children (and $\mathcal{O}(n)$ parents). Therefore, a total of $\mathcal{O}(n)$ evaluations of the for-loop on line 2 of Algorithm 1 is required. Resulting is a linear complexity $\mathcal{O}(n)$.

Backsubstitution Complexity: In an acyclic graph with n nodes there are $\mathcal{O}(n)$ children and $\mathcal{O}(n)$ parents. Therefore, a total of $\mathcal{O}(n)$ evaluations of the for-loops on lines 3 and 9 of Algorithm 2 is required. Resulting is a linear complexity $\mathcal{O}(n)$.

Articulated Mechanism Example

The comparison of dense and sparse LDU decomposition for the example in Fig. 2 is shown in Fig. 3.

$$\begin{aligned}
 \text{(a)} \quad & \begin{pmatrix} \mathbf{D}_1 & 0 & 0 & 0 & 0 & \mathbf{c}'_{61} & 0 & 0 & \mathbf{c}'_{91} \\ 0 & \mathbf{D}_2 & 0 & 0 & 0 & \mathbf{c}'_{62} & \mathbf{c}'_{72} & \mathbf{c}'_{82} & 0 \\ 0 & 0 & \mathbf{D}_3 & 0 & 0 & 0 & \mathbf{c}'_{73} & 0 & 0 \\ 0 & 0 & 0 & \mathbf{D}_4 & 0 & 0 & 0 & \mathbf{c}'_{84} & 0 \\ 0 & 0 & 0 & 0 & \mathbf{D}_5 & 0 & 0 & 0 & \mathbf{c}'_{95} \\ \mathbf{c}_{61} & \mathbf{c}_{62} & 0 & 0 & 0 & \mathbf{D}_6 & \bullet & \bullet & \bullet \\ 0 & \mathbf{c}_{72} & \mathbf{c}_{73} & 0 & 0 & \bullet & \mathbf{D}_7 & \bullet & \bullet \\ 0 & \mathbf{c}_{82} & 0 & \mathbf{c}_{84} & 0 & \bullet & \bullet & \mathbf{D}_8 & \bullet \\ \mathbf{c}_{91} & 0 & 0 & 0 & \mathbf{c}_{95} & \bullet & \bullet & \bullet & \mathbf{D}_9 \end{pmatrix} \\
 \text{(b)} \quad & \begin{pmatrix} \mathbf{D}_5 \mathbf{c}'_{95} & 0 & 0 & 0 & 0 & 0 & 0 & 0 & 0 \\ \mathbf{c}_{95} \mathbf{D}_9 & 0 & 0 & 0 & 0 & 0 & 0 & 0 & \mathbf{c}_{91} \\ 0 & 0 & \mathbf{D}_4 \mathbf{c}'_{84} & 0 & 0 & 0 & 0 & 0 & 0 \\ 0 & 0 & \mathbf{c}_{84} \mathbf{D}_8 & 0 & 0 & 0 & \mathbf{c}_{82} & 0 & 0 \\ 0 & 0 & 0 & \mathbf{D}_3 \mathbf{c}'_{73} & 0 & 0 & 0 & 0 & 0 \\ 0 & 0 & 0 & \mathbf{c}'_{73} \mathbf{D}_7 & \mathbf{c}_{72} & 0 & 0 & 0 & 0 \\ 0 & 0 & 0 & \mathbf{c}'_{82} & 0 & \mathbf{c}'_{72} \mathbf{D}_2 & \mathbf{c}'_{62} & 0 & 0 \\ 0 & 0 & 0 & 0 & 0 & 0 & \mathbf{c}_{62} \mathbf{D}_6 & \mathbf{c}_{61} & 0 \\ 0 & \mathbf{c}'_{91} & 0 & 0 & 0 & 0 & 0 & \mathbf{c}'_{61} \mathbf{D}_1 & 0 \end{pmatrix}
 \end{aligned}$$

Fig. 3: Matrices for the mechanism in Fig. 2 with matching color scheme. Fill-in indicated with “•”. (a) Unordered matrix with fill-in after LDU decomposition. (b) Rearranged matrix without fill-in after LDU decomposition.

The matrices in Fig. 3 have off-diagonal entries only at the intersection of directly connected nodes. For the example mechanism in Fig. 2, the diagonal entries \mathbf{D}_1 to \mathbf{D}_5 are the derivatives of the dynamics \mathbf{d} of each body, and the off-diagonal entries \mathbf{c}_{ij} are the equality constraint derivatives representing joints between two bodies. Note that when processing the matrix in the wrong order, so-called fill-in is created. This fill-in occurs at the off-diagonals of nodes indirectly connected through a node that is processed before it becomes a leaf. Since fill-in must also be processed in the decomposition and backsubstitution, linear complexity is no longer achieved.

Environment Contact Example

A direct result from the linear-complexity property for acyclic graphs is the following. Mechanisms without kinematic loops and only environment contact,

i.e., no contact between bodies, correspond to acyclic graphs and, therefore, have linear complexity in the number of bodies and contact points. Consider the exemplary mechanism, graph, and matrix in Fig. 4.

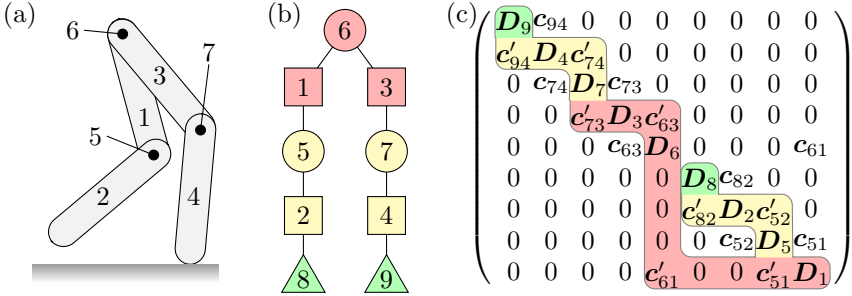


Fig. 4: (a) A walking mechanism with four links, three joints, and two contact points. (b) A graph representing the mechanism. (c) The corresponding rearranged matrix without fill-in after decomposition.

Since all environment contacts are leaves in the graph, adding contact points leads to linear scaling with the correct processing order. This result is especially interesting for bipedal or quadrupedal walking robots.

4.2 Reduced-Fill-In Algorithm

If the graph of a mechanism has cycles, fill-in can generally no longer be avoided entirely since nodes of a cycle are never leaves. However, by processing the leaves attached to a cycle first, the amount of fill-in is reduced. As an example, the mechanism from Fig. 2 is modified to contain a kinematic loop, displayed in Fig. 5.

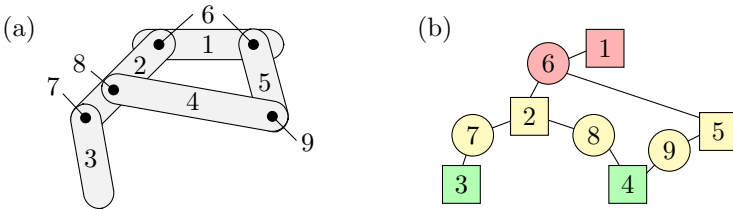


Fig. 5: (a) A mechanism with five links and four joints containing a kinematic loop. (b) A cyclic graph representing the mechanism and its matrix.

Note that for computational reasons two joints are combined into node 6 since these two joints form the beginning of the kinematic loop. Such loop-openers are also found with the depth-first search since they are simply the first and last joint in a detected loop. In the algorithms, a distinction is made

between nodes that are part of a cycle and nodes that are not. This distinction is also determined by the depth-first search.

Since any square matrix can be represented by a (potentially cyclic) graph, the following algorithms are applicable to all such matrices. In the case of mechanical systems, they can be used for all components defined in Section 2. The sparse decomposition for such systems is formulated in Algorithm 3 and the backsubstitution in Algorithm 4.

Algorithm 3 Sparse In-Place LDU Decomposition, Complexity $\mathcal{O}(n + kn^2)$

```

1: for  $i \in \text{list}$  do ▷ list from DFS
2:   for  $c_1 \in \text{acyclic\_children}(i)$  do ▷ children not in a cycle
3:      $F_{i,c_1} \leftarrow F_{i,c_1} F_{c_1,c_1}^{-1}$ 
4:      $F_{c_1,i} \leftarrow F_{c_1,c_1}^{-1} F_{c_1,i}$ 
5:      $F_{i,i} \leftarrow F_{i,i} - F_{i,c_1} F_{c_1,c_1} F_{c_1,i}$ 
6:   end for
7:   for  $c_1 \in \text{cyclic\_children}(i)$  do ▷ successors of  $i$  in a cycle started at  $i$ 
8:     for  $c_2 \in \text{cyclic\_children}(i)$  do
9:       if  $c_1 == c_2$  then
10:        break
11:       else if  $c_2 \notin \text{all\_children}(c_1)$  then ▷ acyclic and cyclic children
12:        continue
13:       else
14:          $F_{i,c_1} \leftarrow F_{i,c_1} - F_{i,c_2} F_{c_2,c_2} F_{c_2,c_1}$ 
15:          $F_{c_1,i} \leftarrow F_{c_1,i} - F_{c_1,c_2} F_{c_2,c_2} F_{c_2,i}$ 
16:       end if
17:     end for
18:      $F_{i,c_1} \leftarrow F_{i,c_1} F_{c_1,c_1}^{-1}$ 
19:      $F_{c_1,i} \leftarrow F_{c_1,c_1}^{-1} F_{c_1,i}$ 
20:      $F_{i,i} \leftarrow F_{i,i} - F_{i,c_1} F_{c_1,c_1} F_{c_1,i}$ 
21:   end for
22: end for

```

Note that all lists in Algorithms 3 and 4 are sorted in the same order as the depth-first search list.

Decomposition Complexity: In a cyclic graph with n nodes and k cycles, there are $\mathcal{O}(n)$ acyclic children and $\mathcal{O}(n)$ acyclic parents. Additionally, there are $\mathcal{O}(n)$ cyclic children and $\mathcal{O}(n)$ loop-opening parents per cycle since each cycle contains at most all nodes and each of these nodes has the same loop-opening parent. Therefore, a total of $\mathcal{O}(n)$ evaluations of the for-loop on line 2 of Algorithm 3 and a total of $\mathcal{O}(kn^2)$ evaluations of the for-loop on line 8 is required. Resulting is a complexity $\mathcal{O}(n + kn^2)$ —quadratic in n and linear in k .

Algorithm 4 Sparse In-Place LDU Backsubstitution, Complexity $\mathcal{O}(n + nk)$

```

1: for  $i \in \text{list}$  do
2:    $\Delta \mathbf{s}_i \leftarrow -\mathbf{f}_i$ 
3:   for  $c \in \text{all\_children}(i)$  do
4:      $\Delta \mathbf{s}_i \leftarrow \Delta \mathbf{s}_i - \mathbf{F}_{i,c} \Delta \mathbf{s}_c$ 
5:   end for
6: end for
7: for  $i \in \text{reverse}(\text{list})$  do
8:    $\Delta \mathbf{s}_i \leftarrow \mathbf{F}_{i,i}^{-1} \Delta \mathbf{s}_i$ 
9:   for  $p \in \text{all\_parents}(i)$  do ▷ direct and loop-opening parents
10:     $\Delta \mathbf{s}_i \leftarrow \Delta \mathbf{s}_i - \mathbf{F}_{c,p} \Delta \mathbf{s}_p$ 
11:   end for
12: end for

```

Backsubstitution Complexity: In a cyclic graph with n nodes and k cycles, there are $\mathcal{O}(n)$ acyclic children, $\mathcal{O}(n)$ acyclic parents, $\mathcal{O}(n)$ cyclic children per cycle, and $\mathcal{O}(n)$ loop-opening parents per cycle. Therefore, a total of $\mathcal{O}(n + nk)$ evaluations of the for-loop on line 3 of Algorithm 4 and a total of $\mathcal{O}(n + nk)$ evaluations of the for-loop on line 9 is required. Resulting is a complexity $\mathcal{O}(n + nk)$ —linear in n and linear in k .

In the worst case of a fully connected graph, i.e., a fully dense matrix, each node has $\mathcal{O}(n)$ cyclic children and parents, resulting in a complexity of $\mathcal{O}(n + n^3)$. However, for real systems, the theoretical complexities are often too conservative. For a system without intersecting cycles, i.e., each node belongs to at most a single cycle, there is a total of $\mathcal{O}(n)$ cyclic children and parents and, therefore, the overall complexity is $\mathcal{O}(n + n^2)$. In case of a constant cycle size there is a total of $\mathcal{O}(k)$ cyclic children and parents and a linear complexity $\mathcal{O}(n + k)$ is obtained. In a combined setting with non-intersecting cycles of fixed size, for example a mechanism with disconnected identical legs made of kinematic loops, there are $\mathcal{O}(n)$ cycles with $\mathcal{O}(1)$ cyclic children and parents each, resulting in a linear complexity $\mathcal{O}(n)$. Improvements on the complexity are theoretically possible, but finding a processing order that creates the minimum amount of fill-in is generally NP-hard [33].

The comparison of dense and sparse decomposition for the example in Fig. 4 with additional dampers at each joint is shown in Fig. 6.

The dampers depend on the relative velocity between the two connected bodies, leading to additional off-diagonal entries. As Fig. 6 shows, with a bad processing order, an almost fully dense matrix is obtained due to fill-in, while the correct processing order creates fill-in only at the off-diagonals of nodes that are part of cycles and the loop-openers.

$$\begin{aligned}
\text{(a)} \quad & \begin{pmatrix} D_1 c'_{12} & 0 & 0 & c'_{51} c'_{61} & 0 & 0 & 0 \\ c_{12} D_2 c'_{32} c'_{42} & \bullet & c'_{62} c'_{72} c'_{82} & 0 \\ 0 & c_{32} D_3 \bullet & \bullet & c'_{73} \bullet & 0 \\ 0 & c_{42} \bullet & D_4 c'_{54} \bullet & \bullet & c'_{84} c'_{94} \\ c_{51} \bullet & \bullet & c_{54} D_5 c'_{65} \bullet & \bullet & c'_{95} \\ c_{61} c_{62} \bullet & \bullet & c_{65} D_6 \bullet & \bullet & \bullet \\ 0 & c_{72} c_{73} \bullet & \bullet & \bullet & D_7 \bullet & \bullet \\ 0 & c_{82} \bullet & c_{84} \bullet & \bullet & \bullet & D_8 \bullet \\ 0 & 0 & 0 & c_{94} c_{95} \bullet & \bullet & \bullet & D_9 \end{pmatrix} \\
\text{(b)} \quad & \begin{pmatrix} D_5 c'_{95} c_{54} & 0 & 0 & 0 & 0 & 0 & c'_{65} c_{51} \\ c_{95} D_9 c_{94} & 0 & 0 & 0 & 0 & \bullet & 0 \\ c'_{54} c'_{94} D_4 c'_{84} & 0 & 0 & c_{42} \bullet & 0 \\ 0 & 0 & c_{84} D_8 & 0 & 0 & c_{82} \bullet & 0 \\ 0 & 0 & 0 & 0 & D_3 c'_{73} c_{32} & 0 & 0 \\ 0 & 0 & 0 & 0 & c'_{73} D_7 c'_{72} & 0 & 0 \\ 0 & 0 & c'_{42} c'_{82} c'_{32} c'_{72} & D_2 c'_{62} c_{21} \\ c_{65} \bullet & \bullet & \bullet & 0 & 0 & c_{62} D_6 c_{61} \\ c'_{51} & 0 & 0 & 0 & 0 & 0 & c'_{21} c'_{61} D_1 \end{pmatrix}
\end{aligned}$$

Fig. 6: Matrices for the mechanism in Fig. 5. (a) Unordered, almost fully dense matrix due to fill-in after LDU decomposition. (b) Rearranged matrix with minimal fill-in after LDU decomposition.

5 Evaluation

The evaluation of the simulator is comprised of three parts. First, the physical accuracy of the variational integrator is analyzed. Then, the runtime and computational complexity of the graph-based algorithms is investigated. Lastly, two application examples for the simulator are given. Comparisons are made to the dynamics simulator *RigidBodyDynamics* [24] as it is written in the same programming language as our integrator, Julia [34]. And also to the widely used simulator *MuJoCo* which is representative for soft constraint handling. In order to solve the integrator equations (27), a basic interior-point method is used and described in Appendix C. Note that the focus of the implementation is on the theoretical properties and not runtime optimization. Nonetheless, even this basic implementation achieves reasonable timing results, benefitting from the easy and modular implementation in maximal coordinates. Code for the simulator¹ and the graph-based system solver² including all experiments and additional examples is available in Julia. All experiments are carried out on an Asus ZenBook with an i7-8565U CPU and 16GB RAM.

5.1 Physical Accuracy

The physical accuracy of the simulator is examined in four scenarios: constraint drift, energy conservation, energy dissipation, and contact violation. A comparison to commonly used alternative implementations is provided for reference. The results are displayed in Fig. 7.

For the constraint drift in Fig. 7 (a), a three-link mechanism forming a kinematic loop is used with link lengths $l_1 = 1\text{m}$, $l_2 = \frac{\sqrt{2}}{2}\text{m}$, $l_3 = 1\text{m}$, masses $m_1 = 1\text{kg}$, $m_2 = \frac{\sqrt{2}}{2}\text{kg}$, $m_3 = 1\text{kg}$, and a time step $\Delta t = 0.01\text{s}$. In minimal coordinates, the loop-closure constraints must be explicitly enforced. In non-variational integrators the dynamics and constraints are formulated

¹<https://github.com/janbruedigam/ConstrainedDynamics.jl>

²<https://github.com/janbruedigam/GraphBasedSystems.jl>

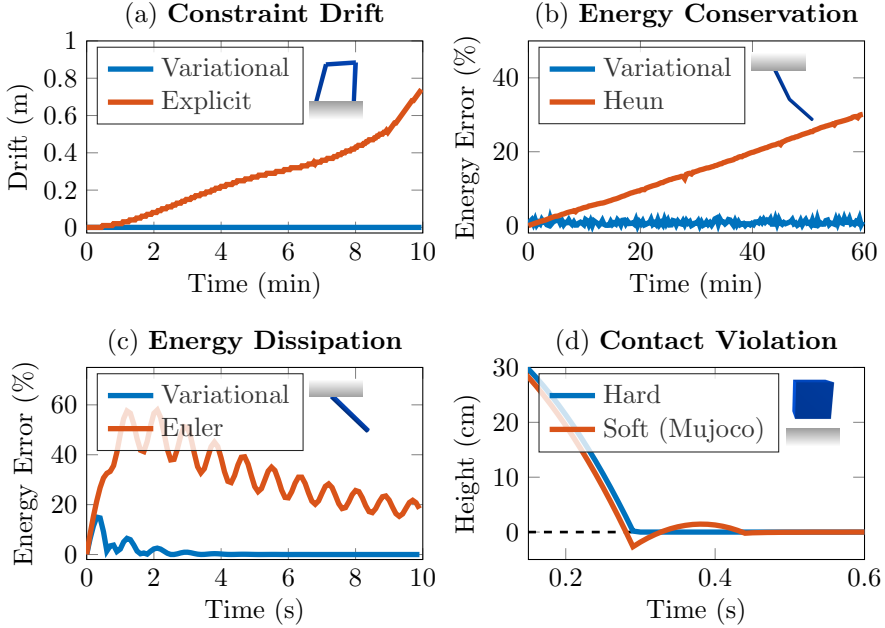


Fig. 7: Evaluation of the physical accuracy of the variational integrator (blue) with comparison (red). (a) Zero constraint drift with variational integrator, drift resulting from explicit 4th-order Runge-Kutta. (b) Bounded energy error with variational integrator for conservative system, increasing error with 2nd-order Runge-Kutta. (c) Small energy error with variational integrator for dissipative system, large error with 1st-order Runge-Kutta. (d) No contact violation for box drop with rigid contact formulation, violation with MuJoCo's soft formulation.

on an acceleration level. Without constraint stabilization [35], i.e., a spring-damper connection, the links of the mechanism start to drift apart. The explicit 4th-order Runge-Kutta-Munte-Kaas integrator [36] exhibits constraint drift without such stabilization. The 1st-order variational integrator prevents constraint drift entirely and does not require constraint stabilization.

The energy conservation in Fig. 7 (b) is evaluated on a frictionless double pendulum with link lengths $l = 1\text{m}$, masses $m = 1\text{kg}$, and a time step $\Delta t = 0.01\text{s}$. Strictly explicit and implicit integrators are not able to conserve energy for conservative mechanical systems. The explicit 2nd-order Runge-Kutta method (Heun's method) injects energy into the system, while the energy error stays bounded for the variational integrator.

Accurate energy dissipation is an important property, for example in passivity-based control approaches [37]. The dissipation behavior in Fig. 7 (c) is evaluated on a damped pendulum with link length $l = 1\text{m}$, mass $m = 1\text{kg}$, joint damping $d = \frac{1}{2}\text{N}\frac{\text{s}}{\text{m}}$ and a time step $\Delta t = 0.1\text{s}$. Euler's method used for

comparison shows poor dissipation behavior in drastically underdamping the pendulum, whereas the variational integrator demonstrates good dissipation performance after a small initial error.

Correct simulation of rigid contacts is crucial for transferring learned or optimized control policies from simulation to a real system. For the comparison of rigid and soft contacts, a cube with edge length $l = 0.5\text{m}$, mass $m = 1\text{kg}$, and time step $\Delta t = 0.01\text{s}$ is dropped from a height (bottom-to-ground) $h = 0.4\text{m}$. MuJoCo’s default solver parameters ($\text{solimp} = (0.9, 0.95, 0.001, 0.5, 2)$, $\text{solref} = (0.02, 1)$) and default Euler integrator are used and result in a ground violation of 2.7cm . We also analyzed drops from other heights up to 1m , which result in similar violations. In contrast, the rigid contact formulation with the variational integrator in maximal coordinates stops $43\mu\text{m}$ above the ground due to the interior-point formulation, which is practically satisfying the constraint.

5.2 Computational Complexity

The evaluation of the computational complexity serves two purposes. We show that the complexity of the graph-based algorithms holds in practice, and by using these algorithms, maximal coordinates can achieve competitive timing results compared to minimal coordinates, despite their larger dimension. For all timings the best result of 100 samples is used to diminish right-skewing computer noise. The linear complexity of the simulator and a comparison to minimal coordinates is shown in Fig. 8. The performance for systems with kinematic loops and comparisons to a dense solver are displayed in Fig. 9.

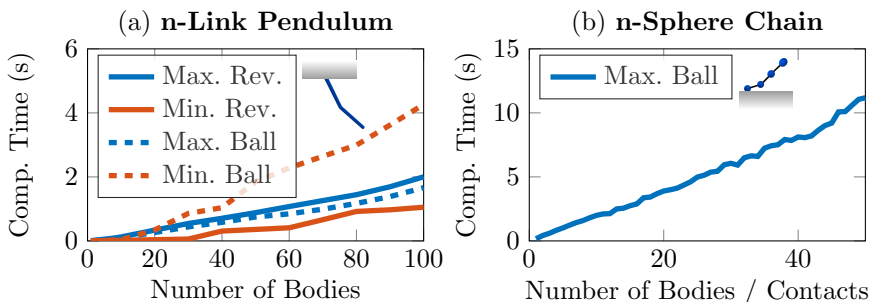


Fig. 8: Computation time comparison for simulating 1000 time steps with our simulator (blue) compared to RigidBodyDynamics (red). (a) n -link pendulum with revolute (solid) and spherical (dashed) joints. (b) n -sphere chain with contacts and spherical joints.

Figure 8 (a) compares the computation time of our simulator with the RigidBodyDynamics simulator for 1000 time steps of n -link pendulums with link length $l = 1\text{m}$, mass $m = 1\text{kg}$, and time step $\Delta t = 0.01\text{s}$. The comparison is made for revolute and spherical (ball-and-socket) joints between the links. The main result is that despite the higher dimension of maximal

coordinates, comparable computation times are achieved. Minimal coordinates are naturally faster for revolute joints, as they have the smallest number of degrees of freedom in minimal coordinates, and the most constraints in maximal coordinates. On the other hand, spherical joints perform worse in minimal coordinates as these joints increase their state dimension and reduce the number of constraints in maximal coordinates. The linear complexity for both minimal and maximal coordinates becomes clearly visible.

In Fig. 8 (b), the linear complexity for contacts is demonstrated for a chain of spheres with radius $r = 0.25\text{m}$, mass $m = 1\text{kg}$, and a time step $\Delta t = 0.01\text{s}$. The spheres are connected by spherical joints. A comparison to RigidBodyDynamics is not possible due to the limited support of contacts. Besides the complexity, this experiment also demonstrates the numerical robustness of the maximal-coordinate approach for treating contacts. We also implemented the experiment in MuJoCo. While faster, MuJoCo with default solver parameters consistently has contact violations of 10cm or more when simulating more than 20 spheres and fails to compute chains consisting of more than 44 spheres. Therefore, a fair comparison is difficult.

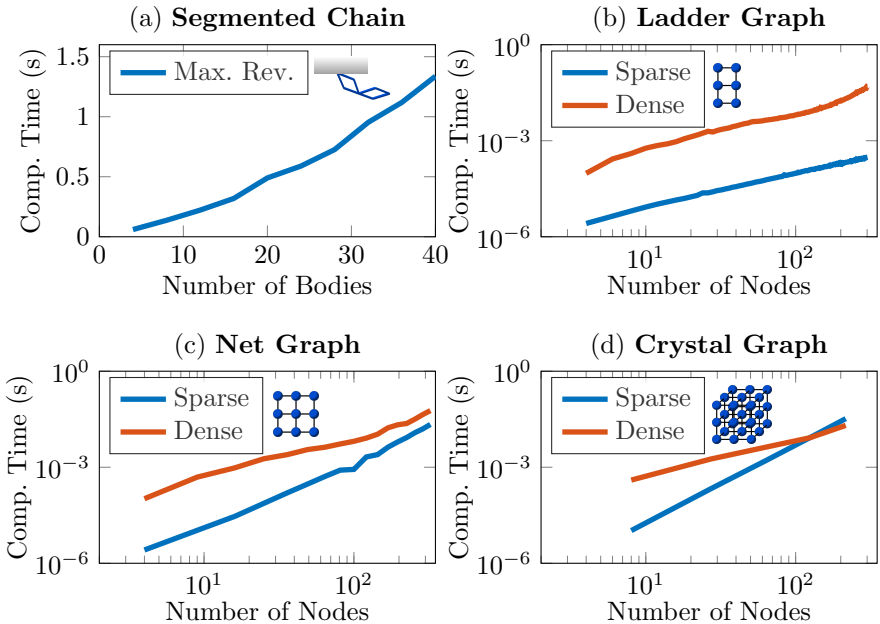


Fig. 9: Evaluation and comparison of our methods (blue) for cyclic structures compared to standard dense implementations (red). (a) Simulation of 1000 time steps of a chain consisting of 4-link segments. (b) Solving of linear system from ladder graph. (c) Solving of linear system from net graph. (d) Solving of linear system from crystal graph.

The computation time for simulating 1000 time steps of a chain of 4-link segments is shown in Fig. 9 (a). The links have a length $l = 1\text{m}$, mass $m = 1\text{kg}$, and time step $\Delta t = 0.01\text{s}$. While no longer fully linear, the increase in computation time for this system is modest due to the reduction of fill-in. A simulation of this system with the RigidBodyDynamics simulator failed for more than one 4-link segment, even for smaller time steps. Numerically, MuJoCo can simulate this system successfully, but with the default solver parameters, the explicit loop-closure constraints introduce high damping into the system, resulting in bad energy conservation behavior.

Comparisons of the sparse graph-based system solver with a dense one are shown in Figs 9 (c) - (d). The ladder graph consists of cycles with four nodes each, and two nodes are shared by two cycles, except for the first and last two nodes. The net graph is a square net of nodes, where inner nodes are part of four cycles, edge nodes part of two, and corner nodes part of one. The crystal graph is a three-dimensional cubic structure of nodes, where inner nodes are part of twelve cycles, surface nodes part of eight, edge nodes part of five, and corner nodes part of three. The graphs with n nodes are represented by matrices with $6n$ entries. The sparse algorithms outperform the dense ones in most cases, often by more than two orders of magnitude. The crystal graph relates to a rather dense matrix, resulting in decreasing advantage of the sparse approach over the dense one, and slightly better performance for $6^3 = 216$ nodes. This last example is an extreme case. The algorithms are aimed at robotic systems which typically have significantly less nodes and cycles, and the sparse performance is convincing for such systems.

5.3 Application Examples

This article focuses on the theoretical foundation for building efficient and physically accurate maximal-coordinate simulators. However, an implementation with a basic interior-point method can already be used for real-world applications. As such application examples, we show that the control parameters for a quadrupedal robot can be learned with a simple sampling-based approach, and how controller gains of an exoskeleton can be personalized to impaired patients in simulation to avoid injury. The quadrupedal robot and learning progress is displayed in Fig. 10. The exoskeleton and resulting torques for original and adapted controller gains is visualized in Fig. 11.

We use the Unitree A1 quadrupedal robot for sampling-based learning. The simulation time step is $\Delta t = 0.001\text{s}$. The learning algorithm is stated in Appendix D. For each episode, a random set of control parameters in a vicinity of the current set of parameters is chosen and a simulation rollout is performed for 10 seconds. In case of progress, i.e., the walking distance increased, this set of parameters is selected as the starting point for new sample draws. The robot learns to walk a distance of more than 12m (average velocity of $1.2\frac{\text{m}}{\text{s}}$) in 100 episodes. Due to the rigid contacts of the simulation, a successful transfer of the learned control parameters to a real system is more likely than with an incorrectly soft contact model.

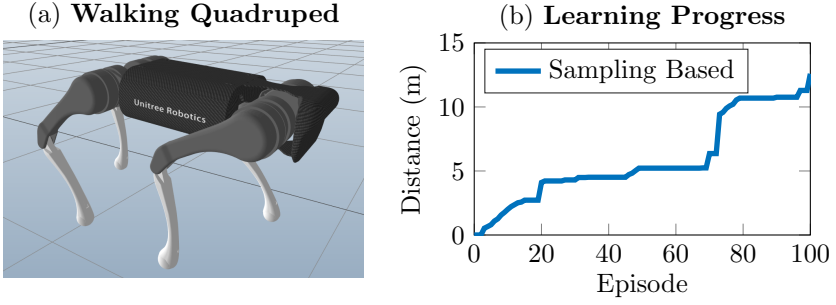


Fig. 10: (a) The trained walking quadruped. (b) Progress for learning to walk.

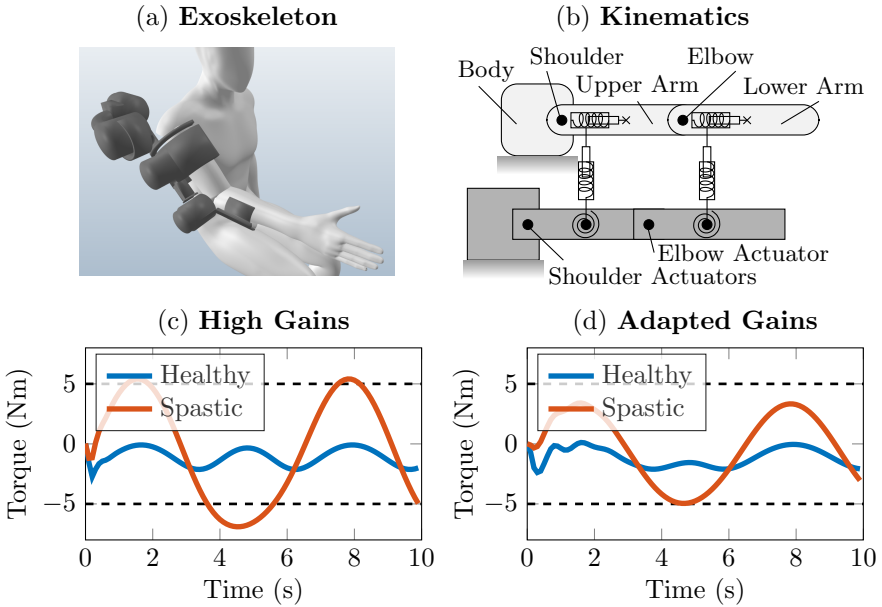


Fig. 11: (a) The donned exoskeleton in simulation. (b) Schematics of the exoskeleton kinematics (not to scale) showing the joints and kinematic loops. Offset between exoskeleton and body exaggerated. (c) Elbow torques during rehabilitation task for high gains. Within limits for healthy patient, exceeding limits for spastic patient. (d) Elbow torques for adapted gains within the limits for both patients.

For the gain tuning, a 4-degrees-of-freedom (DoF) exoskeleton for an arm is used. Three DoF actuate the shoulder and upper arm, one DoF the elbow and lower arm. The attachments of upper and lower arm are modelled as two 3-DoF spring-damper joints with two translational and one rotational

DoF. As a result, there are two connected kinematic loops in the mechanism. Commonly, attachments between exoskeleton and human body are modelled as pure spring-damper connections without joints to avoid such kinematic loops, for example in [2]. However, such models are not necessarily correct. For the exoskeleton application, we assume a healthy and a spastic patient that perform a rehabilitation routine in the exoskeleton. The shoulder and elbow flexion/extension joints are supposed to follow sinusoidal trajectories (see Appendix D). A limit of 5Nm is assumed to be a comfortable elbow torque for the patients. While the original gains stay within these limits for the healthy patient, they are exceeded for the spastic patient. By tuning the gains in simulation, an adapted set of gains adhering to the torque limits for both patients is found. With this approach, uncomfortable and potentially harmful tuning on a real patient can be avoided or at least reduced. The modelling accuracy including proper kinematic loops should provide closer estimates of the controller gains for the real system.

6 Conclusions

This article introduces a maximal-coordinate variational integrator and efficient graph-based solver for simulating mechanical systems with common components such as springs and dampers, actuated joints, and contacts with friction. Besides the theoretical formulation of the integrator and solver algorithms, an application-ready implementation of the simulator is provided as open-source code.

Building maximal-coordinate simulators on variational integrators is useful not just for the conservation properties and physical accuracy, but also for avoiding constraint drift in the naturally constrained formulation. The increased state dimension is treated with efficient numerical solver algorithms which reduce the computational complexity in theory, and render the simulator useable in practice for a variety of applications. Additionally, it appears that the formulation in maximal coordinates increases the numerical robustness and allows for the simulation of systems with contacts or kinematic loops that other simulators in minimal coordinates fail to compute.

Because of the simple modular formulation in maximal coordinates, additional components can be added to the integrator, such as a nonlinear friction model, joint limits, or physically-correct elastic contacts. The graph-based nature of the solver algorithms also opens up the possibility of parallelizing computations on different branches of a graph.

Acknowledgments. The authors would like to thank Petar Bevanda for his help in preparing the manuscript, as well as Marko Galic and Jana Janeva for their implementation help.

Appendix A Quaternions

We use quaternions as rotation representations since they are globally non-singular, as opposed to three-parameter representations, and numerically efficient having only four parameters, unlike, for example, rotation matrices with nine parameters.

A.1 Notation

We write quaternions as a stacked vector,

$$\mathbf{q} = \begin{bmatrix} q_s \\ q_{v_1} \\ q_{v_2} \\ q_{v_3} \end{bmatrix} = \begin{bmatrix} q_s \\ \mathbf{q}_v \end{bmatrix} \in \mathbb{R}^4, \quad (\text{A1})$$

where q_s and \mathbf{q}_v are the scalar and vector parts, respectively. We follow the Hamilton convention with a local-to-global rotation action. In this convention, a quaternion \mathbf{q} maps vectors from the local to the global frame, whereas its inverse maps from the global to the local frame.

Notation (A1) allows for a simple formulation of the basic operations conjugate, inverse, and multiplication:

$$\text{Conjugate:} \quad \mathbf{q}^C = \begin{bmatrix} q_s \\ -\mathbf{q}_v \end{bmatrix} \quad (\text{A2a})$$

$$\text{Inverse:} \quad \mathbf{q}^{-1} = \frac{\mathbf{q}^C}{\|\mathbf{q}\|} \quad (\text{A2b})$$

$$\text{Multiplication:} \quad \mathbf{q} \cdot \mathbf{p} = \begin{bmatrix} q_s p_s - \mathbf{q}_v^\top \mathbf{p}_v \\ q_s \mathbf{p}_v + p_s \mathbf{q}_v + \mathbf{q}_v \times \mathbf{p}_v \end{bmatrix} \quad (\text{A2c})$$

Note that, for unit quaternions, $\mathbf{q}^C = \mathbf{q}^{-1}$, and that the \times operator indicates the standard cross product of two vectors.

Three other common operations are expanding a vector $\mathbf{x} \in \mathbb{R}^3$ into a quaternion, retrieving the vector part from a quaternion, and constructing a skew-symmetric matrix from a vector $\mathbf{x} \in \mathbb{R}^3$ to form the cross product as a matrix-vector product:

$$\text{Expand vector:} \quad \mathbf{x}^\wedge = \begin{bmatrix} 0 \\ \mathbf{x} \end{bmatrix} \quad (\text{A3a})$$

$$\text{Retrieve vector:} \quad \mathbf{q}^\vee = \mathbf{q}_v \quad (\text{A3b})$$

$$\text{Skew-symmetric matrix:} \quad \mathbf{x}^\times = \begin{bmatrix} 0 & -x_3 & x_2 \\ x_3 & 0 & -x_1 \\ -x_2 & x_1 & 0 \end{bmatrix} \quad (\text{A3c})$$

The cross product of two vectors can then be written as $\mathbf{x}_1 \times \mathbf{x}_2 = \mathbf{x}_1^\times \mathbf{x}_2$.

To simplify calculations with quaternions, we introduce the following four matrices with the identity matrix $\mathbf{I}_{3 \times 3} \in \mathbb{R}^{3 \times 3}$:

$$\mathbf{T} = \begin{bmatrix} 1 & \mathbf{0}^\top \\ \mathbf{0} & -\mathbf{I}_{3 \times 3} \end{bmatrix} \in \mathbb{R}^{4 \times 4}, \quad (\text{A4a})$$

$$\mathbf{L}(\mathbf{q}) = \begin{bmatrix} q_s & -\mathbf{q}_v^\top \\ \mathbf{q}_v & q_s \mathbf{I}_{3 \times 3} + \mathbf{q}_v^\times \end{bmatrix} \in \mathbb{R}^{4 \times 4}, \quad (\text{A4b})$$

$$\mathbf{R}(\mathbf{q}) = \begin{bmatrix} q_s & -\mathbf{q}_v^\top \\ \mathbf{q}_v & q_s \mathbf{I}_{3 \times 3} - \mathbf{q}_v^\times \end{bmatrix} \in \mathbb{R}^{4 \times 4}, \quad (\text{A4c})$$

$$\mathbf{V} = \begin{bmatrix} \mathbf{0} & \mathbf{I}_{3 \times 3} \end{bmatrix} \in \mathbb{R}^{3 \times 4}. \quad (\text{A4d})$$

With these matrices all required quaternion operations can be written as matrix-vector products for which the standard rules of linear algebra hold:

$$\mathbf{q}_1 \cdot \mathbf{q}_2 = \mathbf{L}(\mathbf{q}_1) \mathbf{q}_2 = \mathbf{R}(\mathbf{q}_2) \mathbf{q}_1, \quad (\text{A5a})$$

$$\mathbf{q}^{-1} = \mathbf{T} \mathbf{q}, \quad (\text{A5b})$$

$$\mathbf{q}^\vee = \mathbf{V} \mathbf{q}, \quad (\text{A5c})$$

$$\mathbf{x}^\wedge = \mathbf{V}^\top \mathbf{x}. \quad (\text{A5d})$$

For example the rotation of a vector \mathbf{x} can be expressed as

$$(\mathbf{q} \cdot \mathbf{x}^\wedge \cdot \mathbf{q}^{-1})^\vee = \mathbf{V} \mathbf{R}(\mathbf{q})^\top \mathbf{L}(\mathbf{q}) \mathbf{V}^\top \mathbf{x}, \quad (\text{A6})$$

where $\mathbf{V} \mathbf{R}(\mathbf{q})^\top \mathbf{L}(\mathbf{q}) \mathbf{V}^\top$ is the rotation matrix formed from \mathbf{q} .

A.2 Derivatives

While quaternions have four parameters, rotations only have three degrees of freedom, and so we use specialized derivatives for quaternion functions following [16, 38].

The rotational gradient of a quaternion-dependent scalar function $f(\mathbf{q})$ is defined as

$$\nabla_{\mathbf{q}}^r f(\mathbf{q}) = \mathbf{V} \mathbf{L}(\mathbf{q})^\top \nabla_{\mathbf{q}} f(\mathbf{q}), \quad (\text{A7})$$

and the rotational Jacobian of a vector-valued function $\mathbf{f}(\mathbf{q})$ as

$$\frac{\partial \mathbf{f}(\mathbf{q})}{\partial^r \mathbf{q}} = \frac{\partial \mathbf{f}(\mathbf{q})}{\partial \mathbf{q}} \mathbf{L}(\mathbf{q}) \mathbf{V}^\top. \quad (\text{A8})$$

A.3 Properties for Dynamics Descriptions

Using quaternions in the description of dynamical systems requires some attention.

Angular Velocity

In continuous time, the quaternion angular velocity is defined as

$$\bar{\omega} = \begin{bmatrix} \bar{\omega}_s \\ \omega \end{bmatrix} = 2\mathbf{L}(\mathbf{q})^\top \dot{\mathbf{q}}, \quad (\text{A9})$$

where $\bar{\omega}_s = 0$. But when using a first-order approximation of $\dot{\mathbf{q}}$,

$$\dot{\mathbf{q}}_k = \frac{\mathbf{q}_{k+1} - \mathbf{q}_k}{\Delta t}, \quad (\text{A10})$$

generally $\bar{\omega}_s \neq 0$. Therefore, $\bar{\omega}_{k,s}$ is defined so that given \mathbf{q}_k and ω_k , \mathbf{q}_{k+1} maintains unit norm. The discretized angular velocity is

$$\begin{aligned} \omega_k &= \left(2\mathbf{q}_k^{-1} \frac{\mathbf{q}_{k+1} - \mathbf{q}_k}{\Delta t} \right)^\vee \\ &= \frac{2}{\Delta t} (\mathbf{q}_k^{-1} \mathbf{q}_{k+1})^\vee. \end{aligned} \quad (\text{A11})$$

Since $\mathbf{q}_k^{-1} \mathbf{q}_{k+1}$ must have unit norm, the constraint on $\bar{\omega}_k$ is

$$\left\| \frac{\Delta t}{2} \bar{\omega}_k \right\|^2 = \left(\frac{\Delta t}{2} \right)^2 \bar{\omega}_{k,s}^2 + \left(\frac{\Delta t}{2} \right)^2 \omega_k^\top \omega_k = 1 \quad (\text{A12})$$

As a result,

$$\bar{\omega}_k = \begin{bmatrix} \bar{\omega}_{k,s} \\ \omega_k \end{bmatrix} = \begin{bmatrix} \sqrt{\left(\frac{2}{\Delta t}\right)^2 - \omega_k^\top \omega_k} \\ \omega_k \end{bmatrix}. \quad (\text{A13})$$

Virtual Work

According to [29, 30], the virtual rotational work is defined as

$$2 \left(\mathbf{L}(\mathbf{q}) \mathbf{V}^\top \boldsymbol{\tau} \right)^\top \mathbf{q}. \quad (\text{A14})$$

When used in the action integral, the $\mathbf{L}(\mathbf{q}) \mathbf{V}^\top$ component serves as a frame transformation and is not part of the variational trajectory. Therefore, when taking the derivative with respect to \mathbf{q} , this component is not differentiated. As a result, the correct derivative of the virtual work is

$$\nabla_{\mathbf{q}_1}^\top 2 \left(\mathbf{L}(\mathbf{q}) \mathbf{V}^\top \boldsymbol{\tau} \right)^\top \mathbf{q} = 2 \mathbf{V} \mathbf{L}(\mathbf{q})^\top \mathbf{L}(\mathbf{q}) \mathbf{V}^\top \boldsymbol{\tau} = 2 \boldsymbol{\tau}. \quad (\text{A15})$$

Appendix B Kinematic Joints

Most of the common joints can be defined by composing a general translational constraint function and a general rotational constraint function. A visualization of the two constraints is given in Fig. B1. This representation based on two general constraint functions also allows for easy extraction of minimal coordinates.

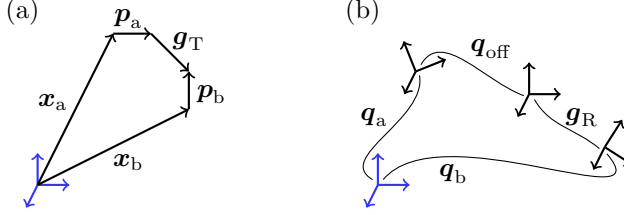


Fig. B1: Visualization of the two general constraints. (a) The relationship of the translational constraint components. (b) The relationship of the rotational constraint components.

B.1 Translational Constraint

The general translational constraint function describes the relative distance of two points relative to the origins of the local frames of two bodies:

$$g_T = (q_a^{-1} \cdot ((x_b^\wedge + q_b \cdot p_b^\wedge \cdot q_b^{-1}) - (x_a^\wedge + q_a \cdot p_a^\wedge \cdot q_a^{-1})) \cdot q_a)^\vee. \quad (B16)$$

The vectors p_a and p_b are defined in the respective local frames, and the resulting relative distance is defined in body a's frame.

In case of only a single body directly connected to the global frame, i.e., $x_a = \mathbf{0}$ and $q_a = \mathbb{1}$ (identity quaternion), we obtain

$$g_T = x_b + (q_b \cdot p_b^\wedge \cdot q_b^{-1})^\vee - p_a. \quad (B17)$$

B.2 Rotational Constraint

The general rotational constraint function describes the relative distance of two local frames of two bodies including a possible offset:

$$g_R = (q_a^{-1} \cdot q_b \cdot q_{off}^{-1})^\vee. \quad (B18)$$

The offset quaternion q_{off} is defined in body a's frame, and the resulting relative rotation is defined in body a's frame as well.

In case of only a single body directly connected to the global frame, i.e., $\mathbf{q}_a = \mathbb{1}$, we obtain

$$\mathbf{g}_R = (\mathbf{q}_b \cdot \mathbf{q}_{\text{off}}^{-1})^\vee. \quad (\text{B19})$$

B.3 Composite Constraints and Minimal Coordinates

To obtain actual joint constraints, the general constraint functions are multiplied with a selection matrix \mathbf{D} indicating the desired constraints. Multiplying the constraint functions with the nullspace matrix \mathbf{C} of \mathbf{D} yields the corresponding minimal coordinates.

The selection matrix \mathbf{D} is calculated by performing singular value decomposition on a skew-symmetric matrix formed from a vector \mathbf{V}_3 :

$$\text{svd}(\mathbf{V}_3^\times) = \mathbf{U}\mathbf{\Sigma}\mathbf{V}^\text{T}. \quad (\text{B20})$$

The matrix \mathbf{V} contains both the original vector \mathbf{V}_3 (sign-adjustment might be necessary), and two perpendicular vectors \mathbf{V}_1 and \mathbf{V}_2 :

$$\mathbf{V} = [\mathbf{V}_1 \ \mathbf{V}_2 \ \mathbf{V}_3] = [\mathbf{V}_{1:2} \ \mathbf{V}_3] \quad (\text{B21})$$

Using the matrices $\mathbf{V}_{1:2}$ and \mathbf{V}_3 , a number of constraint functions $\mathbf{D}^\text{T}\mathbf{g}$ can be created, with the meaning depending on \mathbf{D} . The different options for \mathbf{D} and the corresponding nullspace matrices \mathbf{C} are stated in Table B1.

Selection Matrix \mathbf{D}	Nullspace Matrix \mathbf{C}	Description
$\mathbf{0}_{3 \times 0} \in \mathbb{R}^{3 \times 0}$	\mathbf{V} or $\mathbf{I}_{3 \times 3} \in \mathbb{R}^{3 \times 3}$	No restrictions
$\mathbf{V}_3 \in \mathbb{R}^{3 \times 1}$	$\mathbf{V}_{1:2} \in \mathbb{R}^{3 \times 2}$	Restricted to plane $\mathbf{V}_{1:2}$
$\mathbf{V}_{1:2} \in \mathbb{R}^{3 \times 2}$	$\mathbf{V}_3 \in \mathbb{R}^{3 \times 1}$	Restricted to axis \mathbf{V}_3
\mathbf{V} or $\mathbf{I}_{3 \times 3} \in \mathbb{R}^{3 \times 3}$	$\mathbf{0}_{3 \times 0} \in \mathbb{R}^{3 \times 0}$	Fully restricted

Table B1: Constraint selection and nullspace matrices.

Mechanical joints are created by using different selection and nullspace matrices for the translational and rotational constraints, and stacking everything as

$$\mathbf{D}^\text{T}\mathbf{g} = \begin{bmatrix} \mathbf{D}_\text{T} & \mathbf{0} \\ \mathbf{0} & \mathbf{D}_\text{R} \end{bmatrix}^\text{T} \begin{bmatrix} \mathbf{g}_\text{T} \\ \mathbf{g}_\text{R} \end{bmatrix} = \begin{bmatrix} \mathbf{D}_\text{T}\mathbf{g}_\text{T} \\ \mathbf{D}_\text{R}\mathbf{g}_\text{R} \end{bmatrix}, \quad (\text{B22a})$$

$$\mathbf{C}^\text{T}\mathbf{g} = \begin{bmatrix} \mathbf{C}_\text{T} & \mathbf{0} \\ \mathbf{0} & \mathbf{C}_\text{R} \end{bmatrix}^\text{T} \begin{bmatrix} \mathbf{g}_\text{T} \\ \mathbf{g}_\text{R} \end{bmatrix} = \begin{bmatrix} \mathbf{C}_\text{T}\mathbf{g}_\text{T} \\ \mathbf{C}_\text{R}\mathbf{g}_\text{R} \end{bmatrix}. \quad (\text{B22b})$$

A list of mechanical joints that can be created with this composition is given in Table B2.

Joint Name	D_T	D_R	C_T	C_R
Fixed	$I_{3 \times 3}$	$I_{3 \times 3}$	$0_{3 \times 0}$	$0_{3 \times 0}$
Prismatic	$V_{1:2}$	$I_{3 \times 3}$	V_3	$0_{3 \times 0}$
Planar, fixed orientation	V_3	$I_{3 \times 3}$	$V_{1:2}$	$0_{3 \times 0}$
Fixed orientation	$0_{3 \times 0}$	$I_{3 \times 3}$	$I_{3 \times 3}$	$0_{3 \times 0}$
Revolute (Hinge)	$I_{3 \times 3}$	$V_{1:2}$	$0_{3 \times 0}$	V_3
Cylindrical	$V_{1:2}$	$V_{1:2}$	V_3	V_3
Planar, rotation along axis	V_3	$V_{1:2}$	$V_{1:2}$	V_3
Rotation along axis, free movement	$0_{3 \times 0}$	$V_{1:2}$	$I_{3 \times 3}$	V_3
Spherical (ball-and-socket)	$I_{3 \times 3}$	$0_{3 \times 0}$	$0_{3 \times 0}$	$I_{3 \times 3}$
Cylindrical, free orientation	$V_{1:2}$	$0_{3 \times 0}$	V_3	$I_{3 \times 3}$
Planar, free orientation	V_3	$0_{3 \times 0}$	$V_{1:2}$	$I_{3 \times 3}$
Floating (unconstrained)	$0_{3 \times 0}$	$0_{3 \times 0}$	$I_{3 \times 3}$	$I_{3 \times 3}$

Table B2: List of joints made of the two general constraint functions.

Joints with $D_R = V_3$ do not appear to have any physical meaning. There are also joints that cannot be describe by this composition, for example helical joints (screws). Nonetheless, they can still be formulated as an equality constraint.

Appendix C Simulator Algorithms

The simulator computes the forward dynamics by solving the system of equations 27 at each time step. An interior-point method is implemented as a solver for this systems. The implementation follows Algorithm 19.1 in [31] which provides more detailed explanations. Pseudo code for the implementation is given in Algorithm 5, and code is available in the open-source implementation (see Section 5).

Algorithm 5 Dynamics Simulator

```

1: function line_search( $\Delta \mathbf{s}, \mathbf{s}^{(0)}$ )
2:    $\Delta \mathbf{s} = \text{feasible\_step}(\Delta \mathbf{s})$  ▷ remain feasible, see [31]
3:    $\alpha = 1$  ▷ step length
4:   while true do
5:      $\mathbf{s}^{(1)} = \mathbf{s}^{(0)} + \alpha \cdot \Delta \mathbf{s}$  ▷ take a scaled step
6:     if  $\text{norm}(f(\mathbf{s}^{(1)})) < \text{norm}(f(\mathbf{s}^{(0)}))$  then ▷ successful
7:       return  $\mathbf{s}^{(1)}$ 
8:     end if
9:      $\alpha = \frac{\alpha}{2}$  ▷ half step length
10:  end while
11: end function
12: function interior_point( $\mathbf{s}_0$ )
13:  while true do ▷ iterative solver (Newton-based)
14:     $\text{solve}(\mathbf{F}(\mathbf{s}^{(0)})\Delta \mathbf{s} = -\mathbf{f}(\mathbf{s}^{(0)}))$  ▷ use algorithms in Section 4
15:     $\mathbf{s}^{(1)} = \text{line\_search}(\Delta \mathbf{s}, \mathbf{s}^{(0)})$ 
16:    if  $\text{norm}(\mathbf{f}(\mathbf{s}^{(1)})) < \text{tolerance}$  then ▷ successful
17:      return  $\mathbf{s}^{(1)}$ 
18:    end if
19:     $\text{update\_barrier}()$  ▷ update barrier paramter, see [31]
20:     $\mathbf{s}^{(0)} = \mathbf{s}^{(1)}$ 
21:  end while
22: end function
23: function simulate( $N, \mathbf{s}_0$ ) ▷ simulate  $N$  steps starting at  $\mathbf{s}_0$ 
24:  for  $k = 0 : N - 1$  do ▷ for each step solve (27)
25:     $\mathbf{s}_{k+1} = \text{interior\_point}(\mathbf{s}_k)$  ▷ current state as initial guess
26:  end for
27: end function

```

Appendix D Application Details

Details on the application examples and pseudo code are given in this appendix. Code is available in the open-source implementation (see Section 5).

Walking Quadruped

The legs of the quadruped follow a sinusoidal trajectory with five parameters. The front right and back left leg follow the same trajectory, and the front left and back right leg follow the same trajectory offset by a period of π . The leg trajectories are tracked with proportional-derivative (PD) controllers. Pseudo code for controlling the gait of the quadrupedal robot is stated in Algorithm 6.

Algorithm 6 Leg Controller

```

1: function leg_controller( $t$ , params)           ▷ params found through learning
2:    $b, a_1, a_2, d_1, d_2 = \text{params}$ 
3:    $\theta_{d1} = a_1 \cdot \cos(20\pi \cdot t \cdot b + 0) + d_1$            ▷ thigh joint angle 1
4:    $\theta_{d2} = a_1 \cdot \cos(20\pi \cdot t \cdot b + \pi) + d_1$          ▷ thigh joint angle 2
5:    $\theta_{d3} = a_2 \cdot \cos(20\pi \cdot t \cdot b - \frac{\pi}{2}) + d_2$        ▷ calf joint angle 1
6:    $\theta_{d4} = a_2 \cdot \cos(20\pi \cdot t \cdot b + \frac{\pi}{2}) + d_2$      ▷ calf joint angle 2
7:   for front_right_leg and back_left_leg do
8:      $\tau_{\text{hip}} = 100 \cdot (0 - \theta_{\text{hip}}) - 5 \cdot \dot{\theta}_{\text{hip}}$            ▷ keep hip joint stiff
9:      $\tau_{\text{thigh}} = 80 \cdot (\theta_{d1} - \theta_{\text{thigh}}) - 4 \cdot \dot{\theta}_{\text{thigh}}$    ▷ track desired angle
10:     $\tau_{\text{calf}} = 60 \cdot (\theta_{d3} - \theta_{\text{calf}}) - 3 \cdot \dot{\theta}_{\text{calf}}$      ▷ track desired angle
11:   end for
12:   for front_left_leg and back_right_leg do
13:      $\tau_{\text{hip}} = 100 \cdot (0 - \theta_{\text{hip}}) - 5 \cdot \dot{\theta}_{\text{hip}}$ 
14:      $\tau_{\text{thigh}} = 80 \cdot (\theta_{d2} - \theta_{\text{thigh}}) - 4 \cdot \dot{\theta}_{\text{thigh}}$ 
15:      $\tau_{\text{calf}} = 60 \cdot (\theta_{d4} - \theta_{\text{calf}}) - 3 \cdot \dot{\theta}_{\text{calf}}$ 
16:   end for
17: end function

```

The idea of the sampling-based learning algorithm is to randomly pick the five gait parameters. If progress is made with these parameters, i.e., the robot walks further than before, then the next sampling will be biased in the successful parameter direction. If no progress is made, new parameters are pick randomly in the vicinity of the current parameters. Pseudo code of the sampling-based learning algorithm for the quadruped is state in Algorithm 7.

Exoskeleton

The exoskeleton tracks a sinusoidal rehabilitation trajectory in the shoulder flexion/extension joint, and in the elbow flexion/extension joint. A PD-controller with variable scaling is used for tracking, and this scaling is manually tuned with the simulation to adhere to the torque limit. Pseudo code of the tracking controller is state in Algorithm 8.

Algorithm 7 Sampling-Based Learning Algorithm

```

1: explore_factor = 0.1                                ▷ scaling for random sample generation
2: bias =  $\mathbf{0}_5$                                        ▷ bias direction for sampling
3:  $\text{params}_0 = \text{params}_1 = [0.1, 0, 1, 0, -1.5]$     ▷ initial parameters for standing
4:  $\text{distance}_0 = \text{distance}_1 = 0$                     ▷ walked distance
5: for episode = 1 : 100 do
6:   if bias ==  $\mathbf{0}_5$  then                               ▷ no improvement in last walk
7:      $\text{params}_1 = \text{params}_1 + \text{explore\_factor} \cdot \text{rand}(5)$ 
8:   else                                                 ▷ improvement in last walk
9:      $\text{params}_1 = \text{params}_1 + 0.002 \cdot \text{rand}(5) + 0.01 \cdot \text{bias}$ 
10:  end if
11:   $\text{distance}_1 = \text{simulate}(\text{quadruped}, \text{params}_1)$     ▷ distance walked in 10s
12:  if  $\text{distance}_1 > \text{distance}_0$  then                    ▷ improvement made
13:     $\text{bias} = \text{normalize}(\text{params}_1 - \text{params}_0)$     ▷ calculate bias direction
14:     $\text{params}_0 = \text{params}_1$ 
15:     $\text{distance}_0 = \text{distance}_1$ 
16:     $\text{explore\_factor} = 0.1$                             ▷ reset exploration factor
17:  else                                                 ▷ no improvement made
18:    bias =  $\mathbf{0}_5$ 
19:     $\text{explore\_factor} = 0.9 \cdot \text{explore\_factor}$     ▷ decrease exploration factor
20:  end if
21: end for

```

Algorithm 8 Exoskeleton Tracking Controller

```

1: function exo_controller( $t, \text{scale}$ )                    ▷ scale is tuned manually
2:    $\theta_{e,d} = -\frac{\pi}{4} + \frac{\pi}{4} \sin(t)$                 ▷ elbow trajectory
3:    $\theta_{s,d} = \frac{\pi}{4} + \frac{\pi}{4} \sin(t)$                 ▷ shoulder trajectory
4:    $\tau_e = \text{scale} \cdot 50 \cdot (\theta_{e,d} - \theta_e) + \text{scale} \cdot 5 \cdot (\dot{\theta}_{e,d} - \dot{\theta}_e)$     ▷ PD-controller
5:    $\tau_s = \text{scale} \cdot 100 \cdot (\theta_{s,d} - \theta_s) + \text{scale} \cdot 10 \cdot (\dot{\theta}_{s,d} - \dot{\theta}_s)$     ▷ PD-controller
6: end function

```

References

- [1] Agarwal, P., Narayanan, M.S., Lee, L.-F., Mendel, F., Krovi, V.N.: Simulation-Based Design of Exoskeletons Using Musculoskeletal Analysis. In: Computers and Information in Engineering Conference, pp. 1357–1364. ASMEDC, Montreal, Canada (2010)
- [2] Kuhn, J., Hu, T., Schappler, M., Haddadin, S.: Dynamics simulation for an upper-limb human-exoskeleton assistance system in a latent-space controlled tool manipulation task. In: International Conference on Simulation, Modeling, and Programming for Autonomous Robots (SIMPAR), pp. 158–165. IEEE, Brisbane, Australia (2018)

- [3] Koenemann, J., Del Prete, A., Tassa, Y., Todorov, E., Stasse, O., Bennewitz, M., Mansard, N.: Whole-body model-predictive control applied to the HRP-2 humanoid. In: International Conference on Intelligent Robots and Systems (IROS), pp. 3346–3351. IEEE, Hamburg, Germany (2015)
- [4] Erez, T., Lowrey, K., Tassa, Y., Kumar, V., Kolev, S., Todorov, E.: An integrated system for real-time model predictive control of humanoid robots. In: International Conference on Humanoid Robots (Humanoids), pp. 292–299. IEEE, Atlanta, United States (2013)
- [5] Andrychowicz, O.M., Baker, B., Chociej, M., Józefowicz, R., McGrew, B., Pachocki, J., Petron, A., Plappert, M., Powell, G., Ray, A., Schneider, J., Sidor, S., Tobin, J., Welinder, P., Weng, L., Zaremba, W.: Learning dexterous in-hand manipulation. *The International Journal of Robotics Research* **39**(1), 3–20 (2020)
- [6] Lee, J., Hwangbo, J., Wellhausen, L., Koltun, V., Hutter, M.: Learning quadrupedal locomotion over challenging terrain. *Science Robotics* **5**(47) (2020)
- [7] Todorov, E., Erez, T., Tassa, Y.: MuJoCo: A physics engine for model-based control. In: International Conference on Intelligent Robots and Systems (IROS), pp. 5026–5033. IEEE, Vilamoura-Algarve, Portugal (2012)
- [8] Freeman, C.D., Frey, E., Raichuk, A., Girgin, S., Mordatch, I., Bachem, O.: Brax - A Differentiable Physics Engine for Large Scale Rigid Body Simulation (2021). <http://github.com/google/brax>
- [9] Tedrake, R., the Drake Development Team: Drake: Model-based design and verification for robotics (2019). <https://drake.mit.edu>
- [10] Coumans, E., Bai, Y.: PyBullet, a Python module for physics simulation for games, robotics and machine learning (2016). <http://pybullet.org>
- [11] Zhao, W., Queralta, J.P., Westerlund, T.: Sim-to-Real Transfer in Deep Reinforcement Learning for Robotics: a Survey. In: Symposium Series on Computational Intelligence (SSCI), pp. 737–744. IEEE, Canberra, Australia (2020)
- [12] Featherstone, R.: Rigid Body Dynamics Algorithms. Springer, Boston, United States (2008)
- [13] Featherstone, R.: An Empirical Study of the Joint Space Inertia Matrix. *The International Journal of Robotics Research* **23**(9), 859–871 (2004)
- [14] Higham, N.J.: Accuracy and Stability of Numerical Algorithms, 2nd edn.

SIAM, Philadelphia, United States (2002)

- [15] Baraff, D.: Linear-time dynamics using Lagrange multipliers. In: *Proceedings of the 23rd Annual Conference on Computer Graphics and Interactive Techniques - SIGGRAPH '96*, pp. 137–146. ACM Press, New Orleans, United States (1996)
- [16] Brüdigam, J., Manchester, Z.: Linear-Time Variational Integrators in Maximal Coordinates. In: *Workshop on the Algorithmic Foundations of Robotics (WAFR)*, pp. 194–209. Springer, Cham, Germany (2020)
- [17] Brüdigam, J., Manchester, Z.: Linear-Quadratic Optimal Control in Maximal Coordinates. In: *International Conference on Robotics and Automation (ICRA)*, pp. 9775–9781. IEEE, Xi'an, China (2021)
- [18] Shield, S., Patel, A.: Minor Change, Major Gains II: Are Maximal Coordinates the Fastest Choice for Trajectory Optimization? In: *International Conference on Intelligent Robots and Systems (IROS)*, pp. 12963–12970. IEEE, Kyoto, Japan (2022)
- [19] Marsden, J., West, M.: Discrete mechanics and variational integrators. *Acta Numerica* **10**, 357–514 (2001)
- [20] Johnson, E.R., Murphey, T.D.: Scalable Variational Integrators for Constrained Mechanical Systems in Generalized Coordinates. *IEEE Transactions on Robotics* **25**(6), 1249–1261 (2009)
- [21] Lee, J., Liu, C., Park, F., Srinivasa, S.: A Linear-Time Variational Integrator for Multibody Systems. In: *Workshop on the Algorithmic Foundations of Robotics (WAFR)*, pp. 352–367. Springer, San Francisco, United States (2016)
- [22] Fan, T., Schultz, J., Murphey, T.: Efficient Computation of Higher-Order Variational Integrators in Robotic Simulation and Trajectory Optimization. In: *Workshop on the Algorithmic Foundations of Robotics (WAFR)*, pp. 689–706. Springer, Mérida, Mexico (2018)
- [23] Manchester, Z., Peck, M.: Quaternion Variational Integrators for Spacecraft Dynamics. *Journal of Guidance, Control, and Dynamics* **39**(1), 69–76 (2016)
- [24] Koolen, T., Deits, R.: Julia for robotics: simulation and real-time control in a high-level programming language. In: *International Conference on Robotics and Automation (ICRA)*, pp. 604–611. IEEE, Montreal, Canada (2019)

- [25] Preclik, T., Eibl, S., Rüde, U.: The maximum dissipation principle in rigid-body dynamics with inelastic impacts. *Computational Mechanics* **62**(1), 81–96 (2018)
- [26] Stewart, D.E., Trinkle, J.C.: An Implicit Time-Stepping Scheme For Rigid Body Dynamics With Inelastic Collisions And Coulomb Friction. *International Journal for Numerical Methods in Engineering* **39**(15), 2673–2691 (1996)
- [27] Wenger, T., Ober-Blöbaum, S., Leyendecker, S.: Constrained Galerkin variational integrators and modified constrained symplectic Runge-Kutta methods. In: *International Conference of Numerical Analysis and Applied Mathematics (ICNAAM)*, Rhodes, Greece (2017)
- [28] Wenger, T., Ober-Blöbaum, S., Leyendecker, S.: Construction and analysis of higher order variational integrators for dynamical systems with holonomic constraints. *Advances in Computational Mathematics* **43**(5), 1163–1195 (2017)
- [29] Baruh, H.: *Analytical Dynamics*. WCB, McGraw-Hill, Boston (1999)
- [30] Shivarama, R., Fahrenthold, E.P.: Hamilton’s Equations With Euler Parameters for Rigid Body Dynamics Modeling. *Journal of Dynamic Systems, Measurement, and Control* **126**(1), 124–130 (2004)
- [31] Nocedal, J., Wright, S.: *Numerical Optimization*. Springer, New York, United States (2006)
- [32] Kwak, J., Hong, S.: *Linear Algebra*, 2nd edn. Birkhäuser, Boston, United States (2004)
- [33] Duff, I., Erisman, A., Reid, J.: *Direct Methods for Sparse Matrices*, 2nd edn. Oxford University Press, Oxford, United Kingdom (2017)
- [34] Bezanson, J., Edelman, A., Karpinski, S., Shah, V.: Julia: A Fresh Approach to Numerical Computing. *SIAM Review* **59**(1), 65–98 (2017)
- [35] Baumgarte, J.: Stabilization of constraints and integrals of motion in dynamical systems. *Computer Methods in Applied Mechanics and Engineering* **1**(1), 1–16 (1972)
- [36] Hairer, E., Lubich, C., Wanner, G.: *Geometric Numerical Integration: Structure-preserving Algorithms for Ordinary Differential Equations*, 2nd edn. Springer, Berlin, Germany (2006)
- [37] Music, S., Hirche, S.: Passive noninteracting control for human-robot team interaction. In: *Conference on Decision and Control (CDC)*, pp. 421–427.

IEEE, Miami Beach, United States (2018)

- [38] Jackson, B.E., Tracy, K., Manchester, Z.: Planning With Attitude. IEEE Robotics and Automation Letters **6**(3), 5658–5664 (2021)